ANL/LWRS-25/2

# Stress Corrosion Cracking and Environmentally Assisted Fatigue Behavior of Additively Manufactured 316L Stainless Steel in Light Water Reactor Environment

Nuclear Science and Engineering Division
Argonne National Laboratory

**ANL/LWRS-25/2**

# Stress Corrosion Cracking and Environmentally Assisted Fatigue Behavior of Additively Manufactured 316L Stainless Steel in Light Water Reactor Environment

*LWRS milestone Report Number: M3LW-25OR0402043*

**Bogdan Alexandreanu, Yiren Chen, Xuan Zhang, and Lin Gao**

**Nuclear Science and Engineering Division, Argonne National Laboratory**

**September 2025**

This page intentionally left blank

## ABSTRACT

This report summarizes research activities conducted at Argonne National Laboratory in support of the development, qualification and certification of additively manufactured (AM) metallic components for the long-term sustainability of light water reactors. In this program, the fatigue, environmentally assisted fatigue, and stress corrosion behavior of AM 316L stainless steel (SS) has been evaluated in a light water reactor (LWR) environment, aiming at facilitating the regulatory acceptance and ultimately adoption of AM components in aging LWRs.

In this fiscal year, the performance of AM 316L in a light water environment was evaluated using material from an industry-produced AM flange printed using an EOS M290 Laser Powder Bed Fusion (LPBF) system. The data complements those obtained from tubing printed and tested at ANL using a Renishaw AM400 LPBF. These geometries are intended to act as surrogates for complex components where nuclear equipment vendors are more likely to consider AM technologies. The porosity of the flange material was measured of approximately 9 mm along the radial direction and was found to be small, 0.09%, with only small variations along that direction. Testing involved SCC initiation, SCC crack growth and EAF of the AM material.

SCC CGR testing revealed that the fatigue and corrosion fatigue CGR response of the industry-built flange material was similar to that of the ANL-built material. Also, both AM alloys proved to be resistant to SCC. Crack initiation testing suggests that machined surface is also resistant to SCC initiation in both industry and ANL builds.

The fatigue performance of AM materials was also evaluated in simulated PWR environment. The fatigue life of the industry-built flange material was similar to that of ANL-built tubing material, and they were both lower than the fatigue lives in air. While cyclic softening dominated the stress evolution for both ANL- and industry-produced AM 316L SS, a short period of cyclic hardening can be seen in industry-produced AM material with post-built solution anneal treatment. Nonetheless, the solution anneal treatment did not improve the fatigue performance of AM 316L SS. Based on the approach proposed in NUREG-6909 for wrought and cast austenitic SSs, the estimated environmental correction factor ($F_{en}$) for AM316L SS is about 3 in PWR water. This value is comparable to those for conventional alloys, suggesting similar environmental effects on fatigue behavior for wrought and AM316L SSs.

# TABLE OF CONTENTS

# LIST OF FIGURES

# LIST OF TABLES

## ABBREVIATIONS

| | |
|---|---|
| AM | Additive Manufacturing |
| AMMT | Advanced Materials and Manufacturing Technologies |
| ANL | Argonne National Laboratory |
| APS | Advanced Photon Source |
| ASME | American Society of Mechanical Engineers |
| ASTM | American Society for Testing and Materials |
| CT | Compact Tension |
| DOE | Department of Energy |
| ECP | Electro-chemical Potential |
| EAF | Environmental Assisted Fatigue |
| JSME | Japanese Society of Mechanical Engineers |
| LPBF | Laser Powder Bed Fusion |
| LWR | Light Water Reactor |
| LWRS | Light Water Reactor Sustainability |
| NRC | Nuclear Regulatory Commission |
| ORNL | Oak Ridge National Laboratory |
| SAM | Strain Amplitude |
| SCC | Stress Corrosion Cracking |
| SS | Stainless Steel |
| CGR | Crack Growth Rate |

## ACKNOWLEDGMENTS

This research was supported through the U.S. Department of Energy's Light Water Reactor Sustainability program, Materials Research Pathway. Materials Research Pathway lead: Dr. Xiang (Frank) Chen.

The authors would also like to express their gratitude to D. Gandy and S. Tate from the Electric Power Research Institute for supplying an AM stainless steel 316L flange piece for testing.

This research used resources of the Advanced Photon Source, a U.S. Department of Energy Office of Science User Facility operated for the DOE Office of Science by Argonne National Laboratory under Contract no. DE-AC02-06CH11357.

The authors gratefully acknowledge the assistance of E. Listwan and J. Listwan in specimen preparation, test set-up and printer operation, and JS. Park, V. Cooley in synchrotron X-ray beamtime experiment and X-ray tomography data analysis.

.

# 1 Introduction

Nuclear power has been the largest source of carbon-free power in the U.S. (and much of the developed world) for almost a half century [1]. As such, in the U.S. today, nuclear power plants of the Light Water Reactor (LWR) design generate ~20% of all electricity, comprising over half of carbon-free electricity generation [2,3]. In order to meet the goal of 400 GW nuclear by 2050, the continued operation of the current fleet is required. EPRI estimates that extending the operating life of the existing nuclear fleet to 80 years will result in a 106% increase in power generation when compared to the current remaining operational licenses [3]. Nevertheless, the extended operating lives will pose new challenges to materials and the fabrication of replacement components.

Metal additive manufacturing (AM) or 3D printing by laser powder bed fusion (LPBF) has the potential to transform the nuclear industry by producing high quality, custom-designed components faster and cheaper, thus helping with extending the operating life and enhancing the performance of the current plants [4,5,6]. The US Nuclear Regulatory Commission (NRC) staff has indicated they expect to approve components using a performance-based approach [7] and that, for a material exposed to a LWR environment, the performance-based approach would include the evaluation of environmental effects such as corrosion, stress corrosion cracking (SCC), and environmental fatigue [7,8].

Type 316 austenitic stainless steel has been widely used in various types of LWRs, hence, it has been an early candidate for AM development. One of the initial and most comprehensive studies attempting to evaluate the performance of AM 316L in LWR environment was conducted by X. Lou et al. [9, 10]. The authors commissioned AM samples as well as post-built treatments designed to reduce porosity in the AM material from an external vendor. The authors found that Hot Isostatic Pressing (HIP) + Solution Annealing (SA) reduces porosity from 0.19% in the stress-relieved only alloy to 0.08%. While SCC testing in water involved both as-built (and heat treated) specimens and 20% cold-worked (post-build treatment) specimens, the latter were emphasized as a means of accelerating the SCC tests. The authors found that, after proper high temperature annealing, AM 316L SS by LPBF exhibits similar SCC growth behavior as its wrought counterpart.

This report summarizes research activities initiated at Argonne National Laboratory in support of the development, qualification and certification of additively manufactured (AM) metallic components to allow for innovative reactor design and licensing. The approach undertaken in this study is different from those of the previous studies in several ways. First, the geometry of the AM-built samples was chosen to be close to that of a component used in a nuclear plant. For example, two SS 316L pieces of tubing – surrogates for component-like structures – were built using LPBF AM at ANL. Additional materials – a flange sector build by Westinghouse – was obtained from EPRI. Second, the initial investigation and testing of these materials focused on the as-built structures where available, as post-built treatments are not always feasible for all components. For this research, a microstructural investigation - with a focus on porosity - was conducted on the materials available, as well as mechanical testing with a focus on cracking by fatigue, corrosion fatigue, and stress corrosion cracking (SCC) in an LWR environment. The results were compared with the known behavior of conventionally-produced alloys.

Chapter 2 describes the alloys used in this study and the experimental facilities used to carry out the performance testing in LWR environment. For this purpose, this fiscal year, the performance of AM 316L in a light water environment was evaluated using material from an industry-produced AM flange printed using a EOS M290 Laser Powder Bed Fusion (LPBF) system. The data complements those obtained from tubing printed and tested at ANL using a Renishaw AM400 LPBF. These geometries are intended to act as surrogates for complex components where nuclear equipment vendors are more likely to consider AM technologies. A microstructural evaluation – with an emphasis on porosity – was conducted. The crack growth testing equipment and experimental approach as well as the Environmental Fatigue apparatus are presented. ANL generally followed a well-established testing protocol that has been employed for a number of years and was reported in previous ANL reports.

Chapter 3 provides findings of the microstructural examinations and the results of the environmentally assisted fatigue (EAF) testing and crack initiation and crack growth rate (CGR) tests of AM 316L from the industry-produced flange in a LWR environment. Complete CGR data sets are provided as a function of testing conditions, and presented as crack advance vs. time plots. The corrosion fatigue and stress corrosion cracking (SCC) crack growth rate response was evaluated in simulated primary coolant, and the results were compared to those obtained on in previous testing on AM 316L as well as those for conventionally-produced alloys. Fatigue lives in air and in LWR environment were obtained at different strain amplitudes and compared with those of wrought SSs.

Chapter 4 provides a discussion of the testing results in the framework provided by the well-established fatigue and corrosion fatigue behavior for these alloys, as well as the industry-proposed disposition curves for crack growth [11]. Following the approach previously developed for wrought and cast SSs, the environmental effect on fatigue life was accounted for with a correction factor.

Finally, Chapter 5 gives a summary of the main findings and conclusions.

# 2 Experiment

## *2.1 Alloys*

### *2.1.1 Alloy 316L tubing produced at ANL*

Two AM 316L tubes intended to act as surrogates for complex components where nuclear equipment vendors are more likely to consider AM technologies, Figure 1, were printed using a Renishaw AM400 LPBF system. The printing parameters are also included in the figure. The chemical composition (wt.%) of SS 316L powder are given in Table 1.

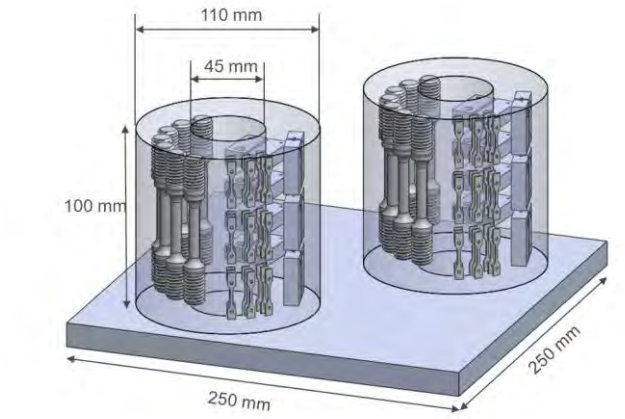


(a)

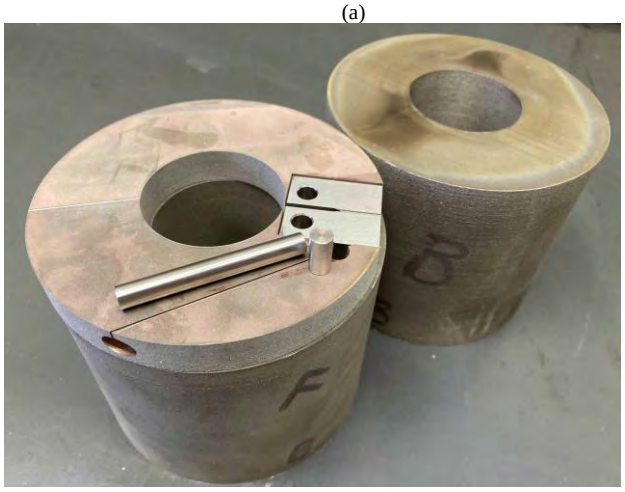

(b)

| Parameter | Value |
|---|---|
| Laser Power | 195 W |
| Layer Thickness | 50 µm |
| Melting Method | Stripe (5mm) |
| Rotation | 67 degrees |
| Exposure Time | 80 µs |
| Point Distance | 60 µm |
| Effective Velocity | 0.75 m/s |
| Hatch Spacing | 110 µm |
| Energy Density | 53.33 J/mm$^3$ |
| Recoater Blade | Rubber |
| Atomization Gas | Argon |
| Build Chamber Atmosphere | Argon |
| Equipment Type | Renishaw AM400 |

(c)

**Figure 1 AM SS 316L tubing (a) as planned, and (b) as printed, with compact tension (CT) specimen for SCC CGR testing in LWR environment. (c) print parameters.**

**Table 1 Chemical composition (wt.%) of SS 316L powder and deposited alloy**

| Alloy | Analysis | C | Mn | Fe | S | P | Si | Cu | Ni | Cr | Mo | Ti | Nb | Co |
|---|---|---|---|---|---|---|---|---|---|---|---|---|---|---|
| Powder | Vendor | 0.022 | 0.90 | Bal. | 0.005 | 0.008 | 0.69 | - | 12.6 | 17.9 | 2.43 | - | - | - |
| AM part | Luvak Inc. | 0.017 | 0.57 | 67.29 | 0.009 | 0.013 | 0.59 | 0.12 | 12.33 | 16.55 | 2.26 | - | - | 0.058 |

The SCC CGR conducted previously involved two specimens: B1-CR-1 and B1-CL-1 from the Alloy 316L tubing produced at ANL. The orientations of these specimens with respect to the tubes are shown in Figure 2.

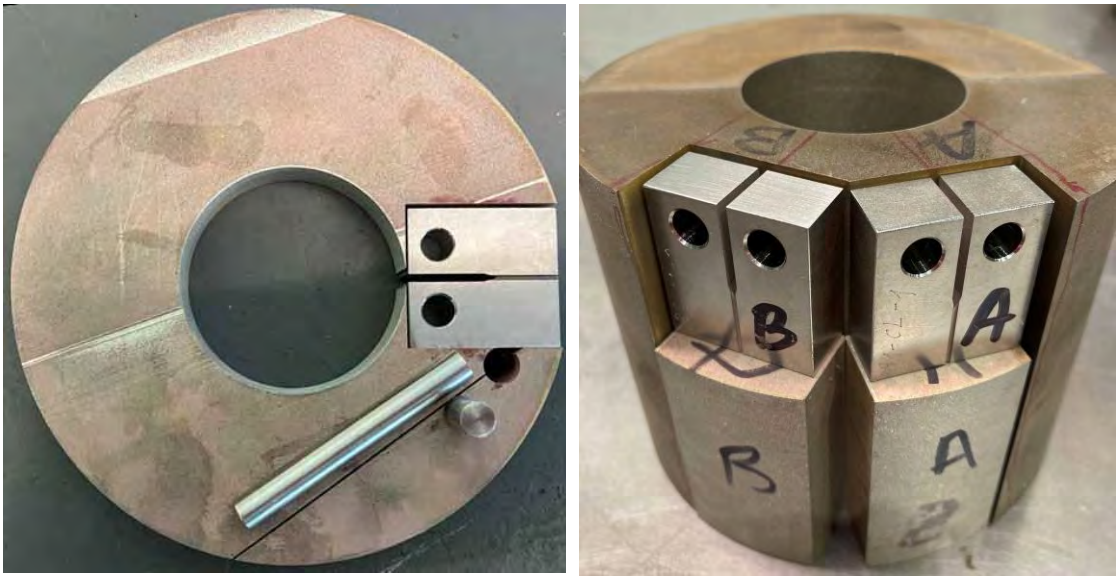


(a) (b)

**Figure 2 (a) CT specimen in the CR orientation for SCC CGR testing in LWR environment; (b) CT specimens in the CL orientation for SCC CGR testing in LWR environment.**

### *2.1.2 Compact tension (CT) specimens printed at ANL*

Compact tension (CT) specimens were printed in order to allow for an evaluation of the crack initiation in AM 316L, Figure 3. The specimens were printed using the Renishaw AM400 LPBF system, with the parameters listed previously. The compositions (wt. %) of SS 316L powder and the AM part are given in Table 1.

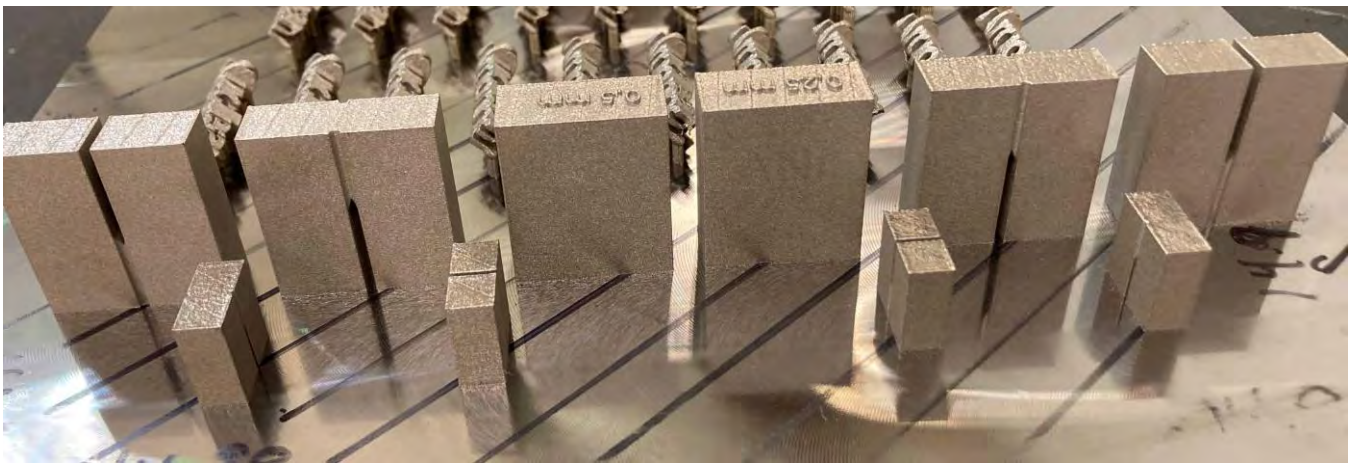

**Figure 3 CGR/crack initiation compact tension specimens printed using the Renishaw AM400 LPBF system.**

### *2.1.3 Alloy 316L Flange produced by industry*

A sector from an AM 316L flange produced by Westinghouse Electric Company (WEC) and used to generate mechanical property data in air for the ASME code case # 20-254 [12] was received from EPRI, Figure 4. The flange was printed using an EOS 290 LPBF system. The printing parameters are also included in the figure. Following printing, the flange was solution annealed (SA) at 2050F (1120ºC) for 2 hours in an argon environment and quenched in water. The chemical composition (wt.%) of SS 316L powder are given in Table 2.

(a)

(b)

| Parameter | Value |
|---|---|
| Laser Power | 214 W |
| Layer Thickness | 40 µm |
| Melting Method | Stripe (12 mm) |
| Rotation | 47 degrees |
| Exposure Time | N/A |
| Point Distance | N/A |
| Effective Velocity | 0.928 m/s |
| Hatch Spacing | 100 µm |
| Energy Density | 57.65 J/mm$^3$ |
| Recoater Blade | Hard (Steel) |
| Atomization Gas | Argon |
| Build Chamber Atmosphere | Argon |
| Equipment Type | EOS M290 |

(c)

**Figure 4 AM 316L flange produced by WEC and used to generate mechanical property data in air for the ASME code case # 20-254 [12] was received from EPRI.**

**Table 2 Chemical composition (wt.%) of SS 316L powder (Praxair TruForm 316-3 Batch No. 22) [12]**

| Alloy | Analysis | C | Mn | Fe | S | P | Si | Cu | Ni | Cr | Mo | N | Cu | O |
|---|---|---|---|---|---|---|---|---|---|---|---|---|---|---|
| Powder | Vendor | 0.012 | 1.24 | Bal. | 0.005 | <0.005 | 0.47 | 0.01 | 12.02 | 17.02 | 2.50 | 0.01 | 0.01 | 0.04 |

Both CGR/crack initiation and fatigue specimens were machined from the flange according to schematic shown in Figure 5.

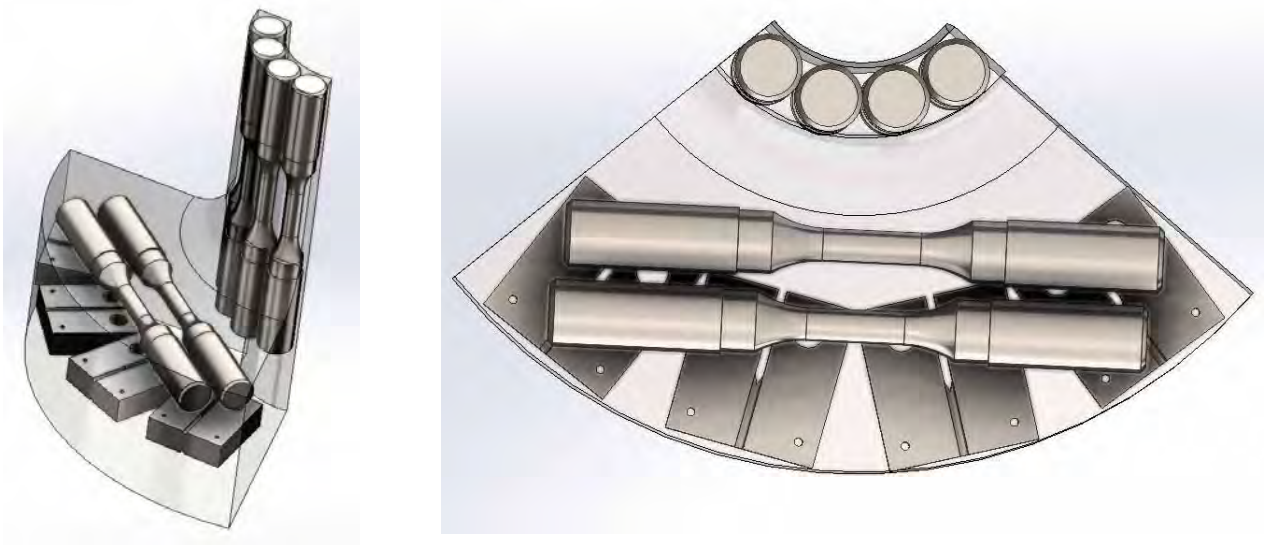

**Figure 5 CGR/crack initiation and fatigue specimens were machined from the AM 316L flange produced by WEC and received from EPRI.**

### *2.2 Porosity measurements at by Tomography at Argonne APS*

Synchrotron micro computed tomography (CT) datasets were collected at the ANL Advanced Photon Source at beamline 1-ID-C. Data were collected with a 52 keV beam using a 5x objective and a FLIR (previously Point Grey Research, Inc.) Grasshopper 3 camera. The reconstructed isotropic voxel pitch was 1.17 μm. Flat field images were collected before and after the scan, and dark field images were collected after the scan only. Projections were collected in 0.2° steps (0-180° total rotation) with 0.2 s integration time per frame. Reconstruction was carried out using a fourierrec algorithm with a Parzen filter using the open-source Python package TomocuPy [13]. Reconstruction included a stripe removal step using the Fourier wavelet method. A final circular mask was applied to remove under-sampled voxels, and reconstructions were outputted as a series of 32-bit float TIFFs.

### *2.3 Mechanical testing in LWR environment*

#### *2.3.1 SCC CGR testing*

The tests conducted under this project were performed on ½-T compact tension (CT) specimens; the geometry of the CT specimens is shown in Figure 6. The CGR tests were conducted in simulated PWR environments at 320°C. The testing protocol was in accordance with ASTM E-647, “Standard Test Method for Measurement of Fatigue Crack Growth Rates,” [14] and ASTM E-1681, “Standard Test Method for Determining a Threshold Stress Intensity Factor for Environment-Assisted Cracking of Metallic Materials under Constant Load” [15].

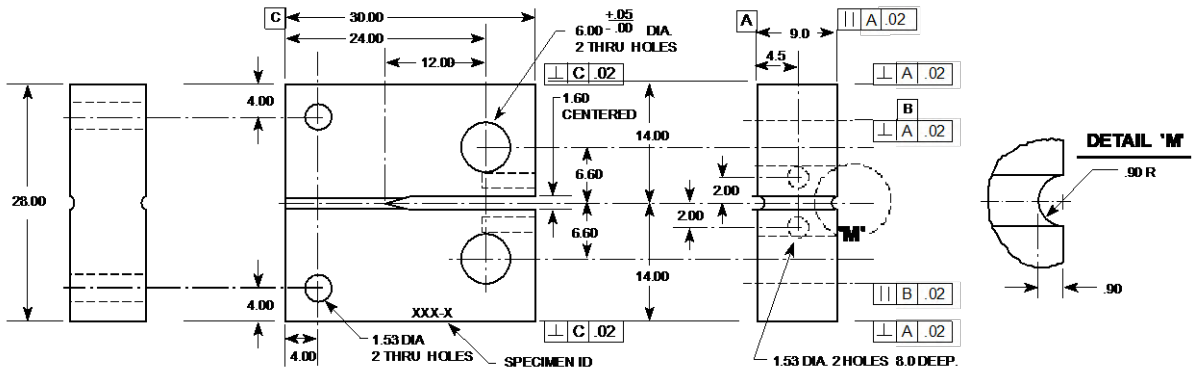


**Figure 6 Configuration of the ½-T CT specimen used for this study. Dimensions are in mm.**

The CGR tests were conducted in test facilities equipped with either 2 or 6-liter stainless steel (SS) autoclaves. Each system has a suite of calibrated instrumentation, including digitally controlled hydraulic loading and load cells, and an independent water loop to maintain a simulated PWR environment with water chemistry monitoring. The test systems are nearly identical except for the maximum load rating of the test frame and the volume of the autoclave vessel. A detailed description of the test system with the 2-liter autoclave is provided in this section.

The 2-liter autoclave test facility allows test temperatures of up to 350°C. Figure 7 is a photograph showing the entire test system. The servo-hydraulic test frame consists of a load train, an autoclave support frame, and autoclave. The hydraulic actuator is mounted on bottom of the test frame, with the load train components located above it. The load cell is located at the bottom of the pull rod. An Instron Model 8800 system is used to control the load on the specimen. The test temperature is maintained by heater bands mounted on the autoclave body.

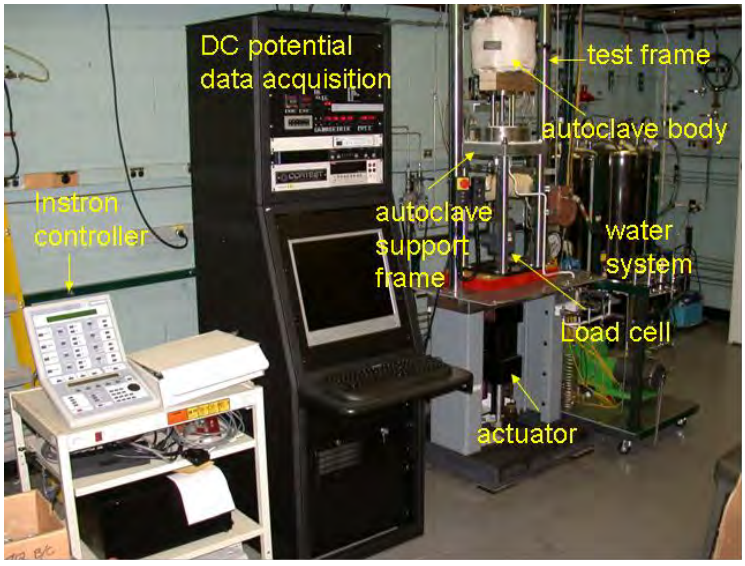


**Figure 7 Layout of the 2-liter SCC test system.**

The autoclave support frame consists of a thick plate supported by four compression rods (Figure 8). The internal load frame that contains the test specimen consists of a top plate supported by three rods. The upper two-piece clevis assembly is fastened to the top plate of the internal load frame, and the lower piece clevis assembly is connected to the pull rod. The specimen to be tested is mounted between the clevises. The specimen and clevises are kept electrically insulated from the load train by using oxidized Zircaloy pins and mica washers to connect the clevises to the rest of the load train. Water is circulated through a port in the autoclave head, which serves both as inlet and outlet. A schematic diagram of the recirculating water system is shown in Figure 9.

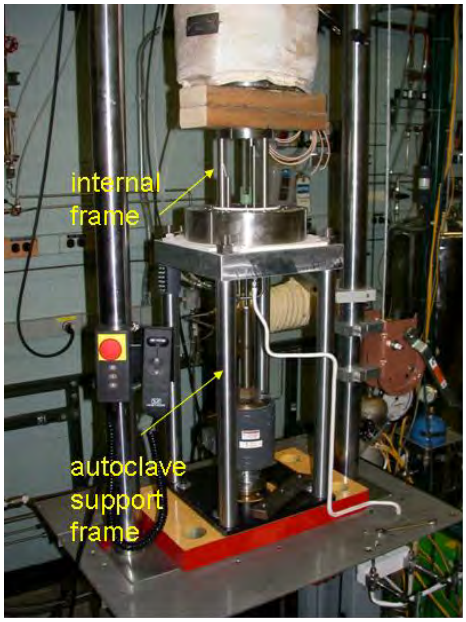


**Figure 8 Photograph of the specimen load train for the 2-liter autoclave.**

The simulated PWR feedwater contains 2 ppm Li as LiOH, 1000 ppm B as $HBO_3$, ≈2 ppm dissolved hydrogen (≈23 $cm^3$/kg), and less than 10 ppb dissolved oxygen (DO) [16]. Water is circulated at relatively low flow rates (15-25 mL/min). The test temperature was 320°C.

Crack extensions are monitored by the reversing-direct current (DC) potential difference method, Figure 10. In this method, a constant DC current is passed through the test specimen and the crack length is measured through the changes in the electrical voltage at the crack mouth. The electrical voltage measured across the crack mouth is related to the unbroken crack ligament resistance through the Ohm's law. Thus, as the crack advances, the length of the unbroken ligament decreases and its resistance increases. In short, as the crack advances the voltage measured across the crack mouth increases. Figure 10 shows a typical configuration of a CT specimen instrumented for crack growth measurements by the DC potential method: the current leads are welded on the top and bottom surfaces of the specimen, and potential leads are welded on the front face of the specimen across the machined notch but on diagonal ends. Also, to compensate for the effects of changes in resistivity of the material with time, an internal reference bar of the same material being tested is installed in series, near the test specimen. The voltage readings across the reference bar are used to normalize potential drop measurements for the CT test specimen. The changes in potential drop measurements for the CT test specimen are transformed into crack advance data using correlations developed for the specimen geometry that is tested. In practice, voltage readings are taken successively as the current is reversed,

and, typically, 800 voltage readings are needed to generate 1 crack advance data point, approximately every 4 min. with a resolution of approximately 1-2 µm [0.039-0.079 mils].

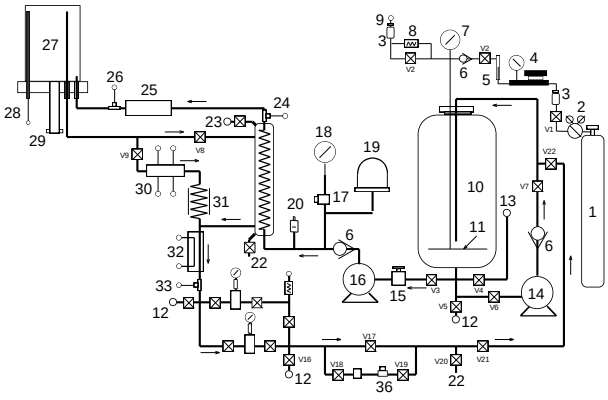

1. COVER GASS SUPPLY TANK
2. TWO-STAGE HIGH-PRESSURE REGULATOR
3. FLASH ARRESTOR
4. LOW-PRESSURE REGULATOR
5. FLOW METER
6. CHECK VALVE
7. COMPOUND VACUUM & PRESSURE GAUGE
8. PRESSURE RELIEF VALVE
9. VENT TO AIR & FLASH ARRESTOR
10. FEEDWATER STORAGE TANK
11. SPARGE TUBE
12. WATER SAMPLE PORT
13. FEEDWATER FILL PORT
14. FEEDWATER TANK RECIRCULATION PUMP
15. SOLENOID VALVE
16. HIGH-PRESSURE PUMP
17. PRESSURE TRANSDUCER
18. HIGH-PRESSURE GAUGE
19. ACCUMULATOR
20. RUPTURE DISC
21. HEAT EXCHANGER (HX)
22. DRAIN
23. SYSTEM BLEED PORT
24. HEAT EXCHANGER OUTLET TC
25. AUTOCLAVE PREHEATER
26. PREHEATER OUTLET TC
27. COMMERCIAL AUTOCLAVE
28. THERMOWELL
29. "BAL SEAL" RETAINER
30. ECP CELL
31. AIR-COOLED COIL
32. WATER COOLED HEAT EXCHANGER
33. BACK-PRESSURE REGULATOR (BPR) INLET TC
34. BPR
35. PH METER
36. CONDUCTIVITY METER

**Figure 9 Schematic diagram of the recirculating 2-liter autoclave system.**

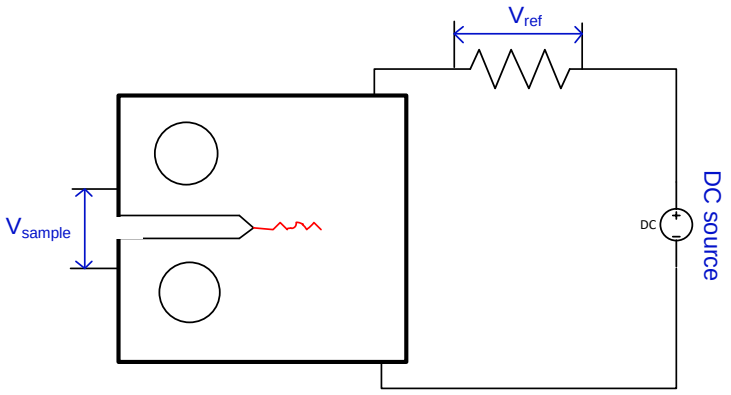


**Figure 10 Principle of crack length measurement by the DC potential method.**

### *2.3.2 SCC initiation testing*

Crack initiation testing was conducted in the same facility used for SCC CGR testing with the purpose of evaluating the resistance of AM 316L to crack initiation. Testing is conducted on specimens that are either machined from the AM-produced component or directly printed. The latter are used for the evaluation of crack initiation from the as-printed surface. For example, the two printed AM316L specimens shown in Figure 11 differ only at the notch, one has the notch "as printed" and the other was machined to the intended to remove the printed surface.. In order to detect crack initiation, the two specimens were instrumented for DC potential and loaded simultaneously. To accelerate the degradation effect(s), the water environment was aerated (8 ppm DO). The aerated, high electro-chemical potential (ECP) condition is a realistic "off-normal" environment believed to occur at restart after a shutdown [17,18].

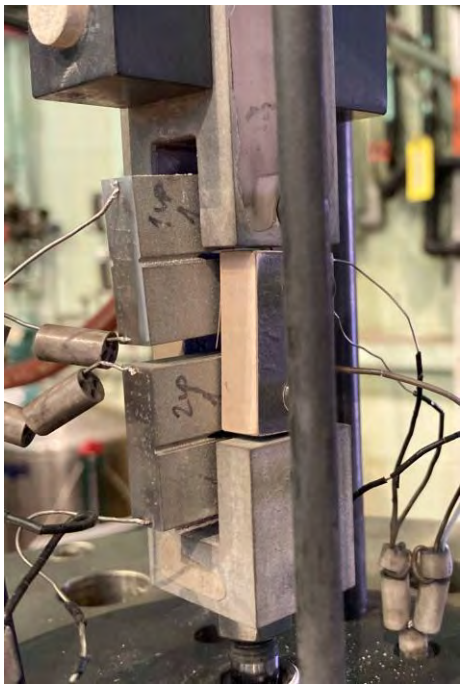

**Figure 11 AM316L printed CT specimens differing only at the notch – "as printed" vs "machined"- instrumented for DC potential and loaded in series.**

### *2.3.3 Fatigue and environmentally assisted fatigue testing*

Two sample geometries were used in this study for fatigue tests conducted in air and in an LWR water environment (i.e., environmentally assisted fatigue, EAF). The sample used for the in-air fatigue tests has a nominal gauge diameter of 0.215" (5.46 mm), a gauge length of 0.64" (16.26 mm), and a total length of 4.0" (101.6 mm), as shown in Figure 12a. For the EAF tests however, a slightly smaller sample geometry was used due to the space limitations of the autoclave. As shown in Figure 12b, both the gauge diameter and length of the EAF sample were approximately 14% smaller than those of the in-air fatigue sample.

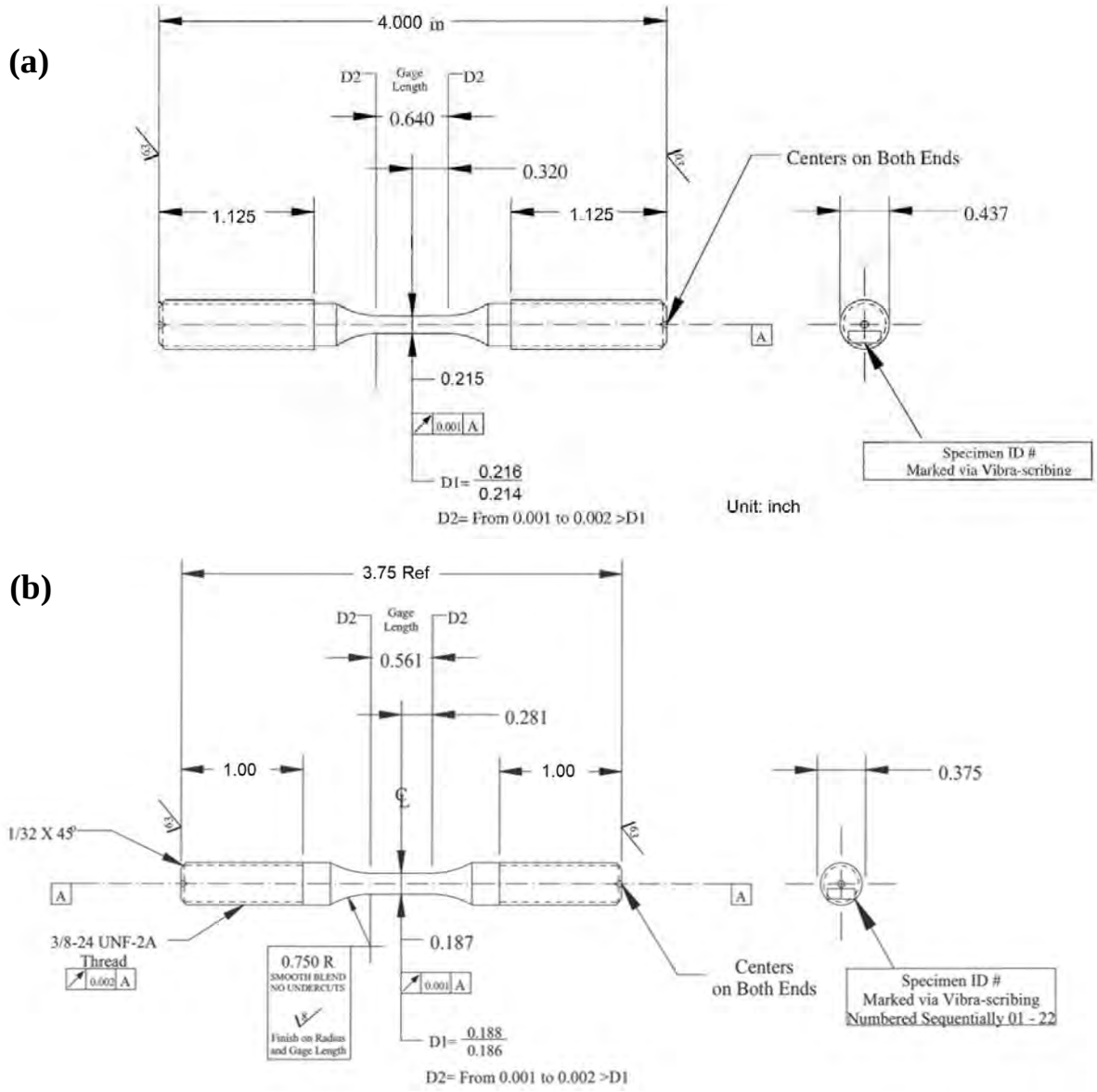


**Figure 12 Schematics of the samples used for the in-air fatigue tests (a), and for the EAF tests in a LWR environment (b). Note that all dimensions in the drawings are in inch.**

For the AM 316L tubes produced by ANL, fatigue samples were sectioned parallel to the build direction (Figure 13). The samples tested in air were taken from the mid-wall plane, whereas the samples tested in water were taken from three circumferential planes across the wall thickness. For the AM 316L flange produced by WEC, fatigue samples were extracted in two orientations -- parallel or perpendicular to the build direction (Figure 5). The sample parallel to the build direction were tested in this Fiscal Year.

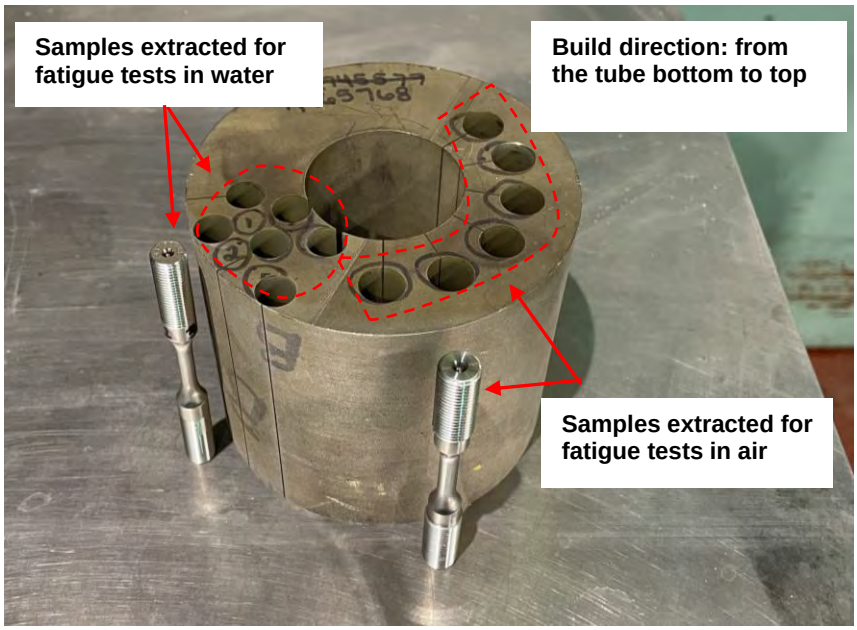


**Figure 13 Locations where the fatigue and EAF samples were extracted from**

Fatigue tests in air were performed per ASTM Standard E606/606M, "Standard Test Methods for Strain-Controlled Fatigue Testing." [19] The tests were carried out on a closed-loop servo-hydraulic test frame equipped with a three-zone split furnace. The test temperature was controlled at 300°C with two pairs of Type-K thermocouples positioned at the top and bottom grips of the specimen. The tests were performed under a stain controlled mode in a fully reversed condition (R = -1). A high-temperature extensometer mounted on the uniform gauge section of the specimen was used for the strain measurement and feedback control. Instron WaveMatrix$^{TM}$ Dynamic Software was used for the test control and data acquisition. The stress-strain hysteresis loop and the maximum and minimum stresses were recorded at different intervals throughout the test. The number of cycles to failure is defined as the number of cycles when the stress amplitude is reduced by approximately 50% of the maximum stress, or the final recorded cycle when an unstable fracture occurs. Figure 14 shows an example of a fatigue test conducted in air. With the AM sample in its as-printed condition, no cyclic hardening was observed, and the sample experienced cyclic softening throughout the test (Figure 14b-c).

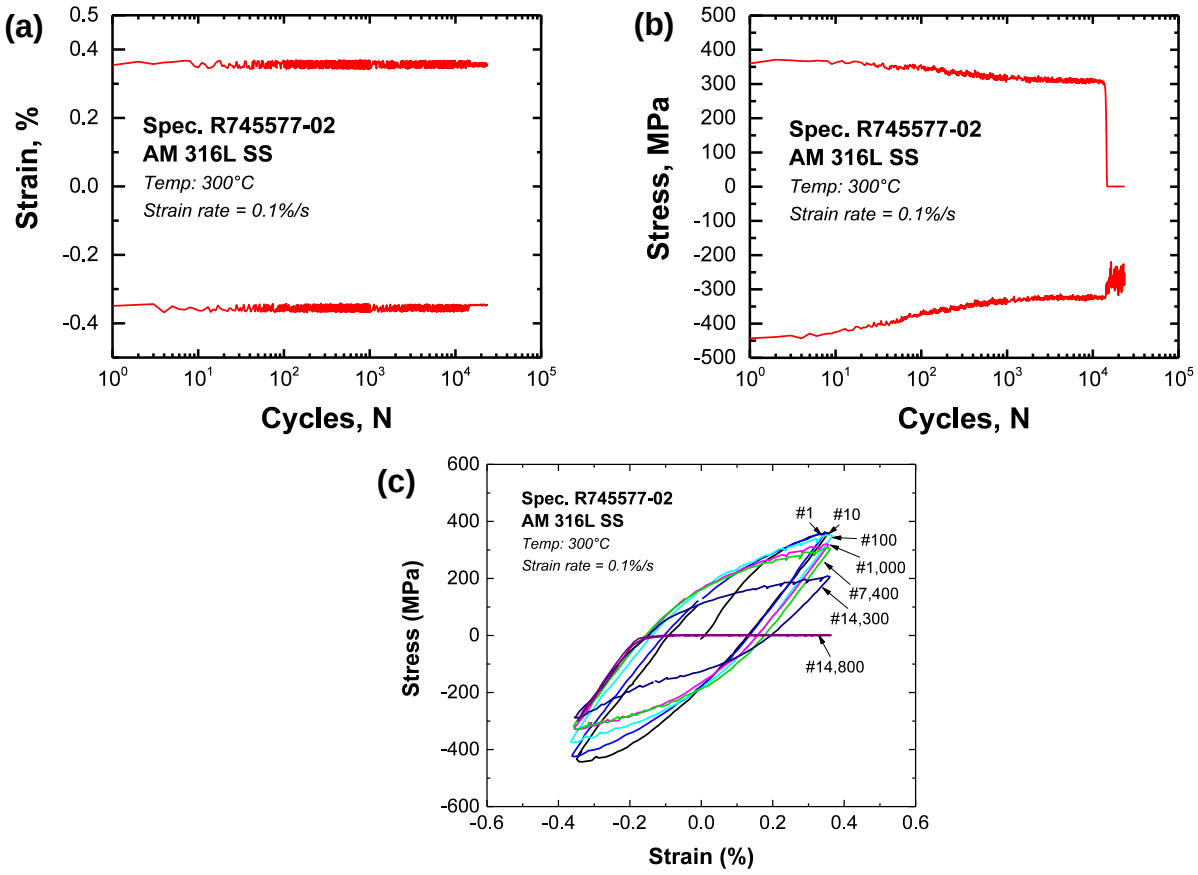


**Figure 14** **The strain (a) and stress (b) profiles, and selected hysteresis loops at different cycles (c) for an in-air fatigue test performed at a strain amplitude of 0.35%.**

Fatigue tests in water were performed with a servo-hydraulic test frame retrofitted with an autoclave and a water recirculation system (shown in Figure 15). The autoclave was constructed of Type 316 SS and had an annular volume of ~12 ml around the sample's gauge section. The water circulation system consisted of a 130-liter retention tank, a high-pressure pump, a heat exchanger, and a preheater as shown in Figure 16. During the tests, simulated PWR water was pressurized to ~1450 psig (~10 MPa) and circulated at a rate of ~10 ml/min through the autoclave. The autoclave temperature was controlled at 300°C. Since the extensometer cannot be used inside the autoclave, the in-water tests were conducted by controlling the pull-rod displacement using a linear variable differential transformer (LVDT) located outside the autoclave. The stress-strain results of the in-air fatigue tests were used to determine the input for the pull-rod displacement of the in-water tests. Note that, with this control mode (referred as "stroke control"), the compliance of the load train outside the sample's gauge also influences to the tests. As a result, the applied strain amplitude or strain rate is not constant. However, given the smaller cross-section area of the gauge compared to that of the rest of load train, most of the applied pull-rod displacement should go to the sample gauge.

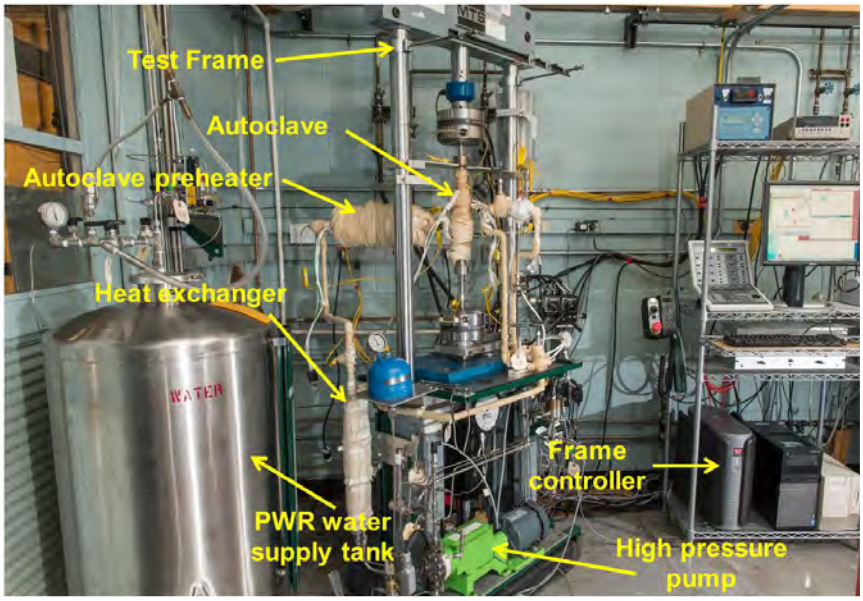


**Figure 15 Fatigue test system equipped with an autoclave and a water circulation system.**

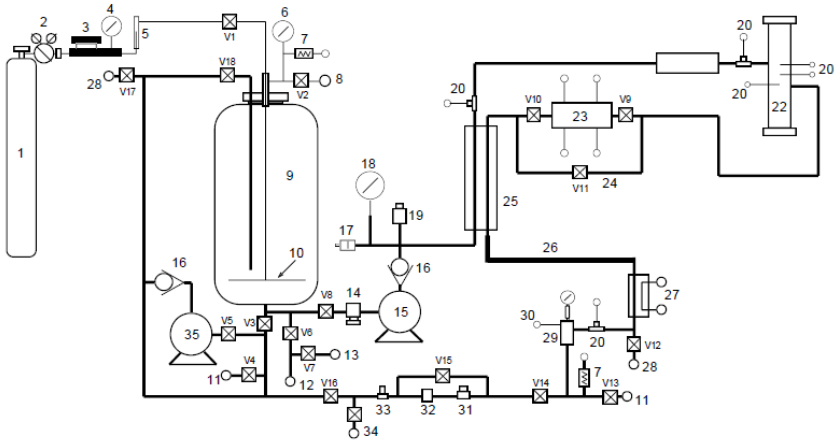

1. COVER GAS SUPPLY TANK
2. HIGH-PRESSURE REGULATOR
3. LOW-PRESSURE REGULATOR
4. PRESSURE GAUGE
5. FLOW METER
6. VACUUM & PRESSURE GAUGE
7. PRESSURE RELIEF VALVE
8. VENT TO ROOM VENTILATION
9. FEEDWATER STORAGE TANK
10. SPARGE TUBE
11. WATER SAMPLE PORT
12. TO 2nd FEEDWATER TANK
13. FEEDWATER FILL PORT
14. SOLENOID VALVE
15. HIGH-PRESSURE PUMP
16. CHECK VALVE
17. RUPTURE DISK
18. HIGH-PRESSURE GAUGE
19. PRESSURE TRANSDUCER
20. THERMOCOUPLE WELL
21. AUTOCLAVE PREHEATER
22. TUBE AUTOCLAVE
23. ECP CELL
24. ECP CELL BYPASS LINE
25. HEAT EXCHANGER
26. LARGER SIZE TUBING
27. WATER COOLED CHILL PLATE
28. SYSTEM BLEED PORT
29. BACK-PRESSURE REGULATOR
30. COMPRESSED AIR LINE
31. CONDUCTIVITY METER
32. PH METER
33. FLOW METER
34. DRAIN
35. RECIRCULATING PUMP
36. RETURN LINE

**Figure 16 Schematic of autoclave water recirculation system for EAF testing.**

# 3 Results

This section describes the results of the microstructural investigation focusing on porosity, and the results of crack initiation testing, crack growth rate (CGR) testing, and environmentally assisted fatigue.

## *3.1 Microstructure*

### *3.1.1 Alloy 316L tubing produced at ANL*

The post-build examination consists of visual inspection and optical metallography. Of high interest is the porosity of the material. The planes of interest were the ones susceptible to crack propagation in an actual component.

Crack growth rate measurements are typically made using CT specimens. Figure 17 [20] shows the nomenclature for CT specimen orientations with respect to a cylindrical product form, such as an extruded control rod drive mechanism (CRDM) nozzle or the AM-produced tubing described in this section. The first letter in the two-letter designation is normal to the propagation plane, and the second gives the direction of propagation:

L – direction of maximum grain flow (axial)
R – radial direction, and
C – circumferential or tangential direction

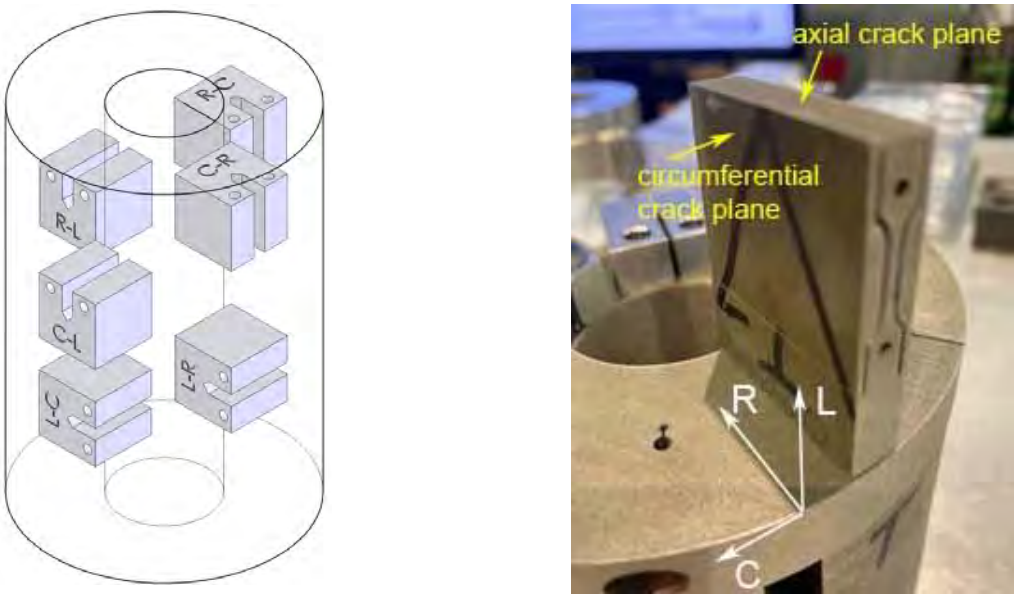


(a) (b)

**Figure 17 (a) Specimen orientations for a cylindrical product form [20]; (b) Photograph showing the planes of interest in the AM 316L tubing.**

Because cracks in plant components can grow in both length and width, the orientation of an in-service crack propagating through-wall can be represented by the C-R or C-L orientations for an axial crack and by the L-R or L-C orientations for a circumferential crack. The R-L and R-C orientations are parallel to

the pressurized surface, often termed the laminar direction; flaws in these orientations have never been observed in service. This is because radial stresses must be in equilibrium with the stress at the surface. The stress at the surface is either zero or compressive and is equal in magnitude to the internal pressure for a pressurized cylinder.

The microstructure in the circumferential plane (parallel to the build direction) is shown in Figure 18. Porosity was observed, and this was analyzed with additional accuracy by tomography at ANL APS.

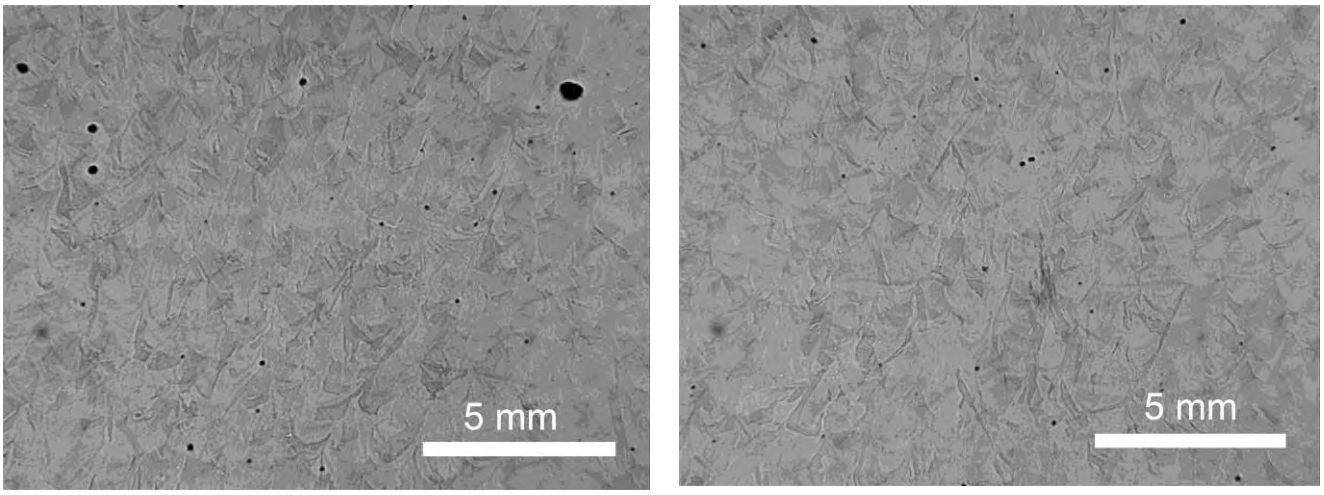


(a) (b)

**Figure 18 Microstructure in the circumferential plane (parallel to the build direction). Build direction is from bottom to top.**

High-energy X-ray tomography – available at Argonne's Advanced Photon Source (APS) was used for a detailed characterization of porosity and micro-cracking, which are critical factors for material's mechanical performance. Figure 19, taken from [21], shows an example of X-ray tomography reconstruction of built-in pores in a LPBF (Laser-Powder Bed Fusion) 316L sample unconnected to this project. The spatial and size distributions of pores were quantitatively determined, and for the example shown, the microstructural information was used to determine the optimum printing parameters for printing.

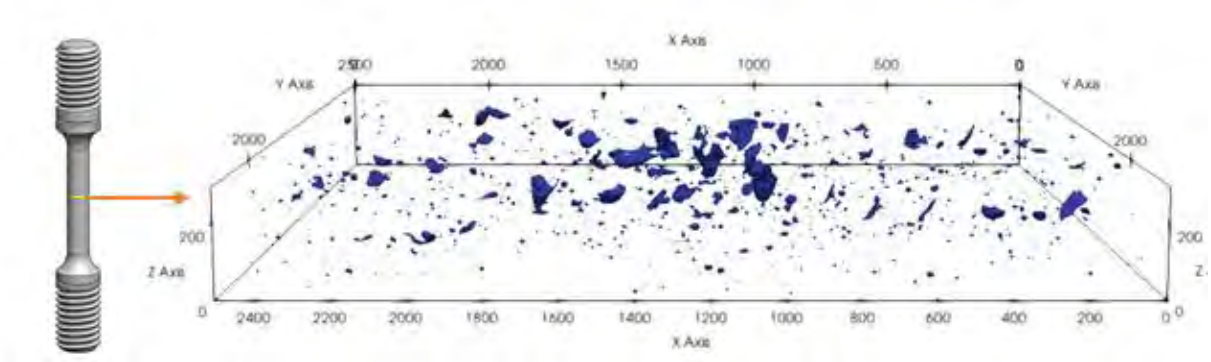


**Figure 19 Synchrotron X-ray tomography of pores in an AM sample; axis labels are in pixel, 1 pix = 4.172 µm. The data from this figure was collected at the Advanced Photon Source at Argonne [21].**

The evaluation of porosity by X-ray Tomography at Argonne APS in the as-built tubing material produced by ANL was conducted in the region to be sampled in SCC CGR test, Figure 20. Figure 20a shows the radial bar for porosity measurement, and the arrow indicates the approximate location of the measurement reported here. This was close to the ID of the tube, and, as already mentioned, representative of the test plane of the CT specimens. The porosity was calculated over a volume of 3.05 $mm^3$, and was found to be 0.06%, close to the HIP + SA condition described in [9]. The average pore size was 7.2 µm (with a 3 µm detection limit).

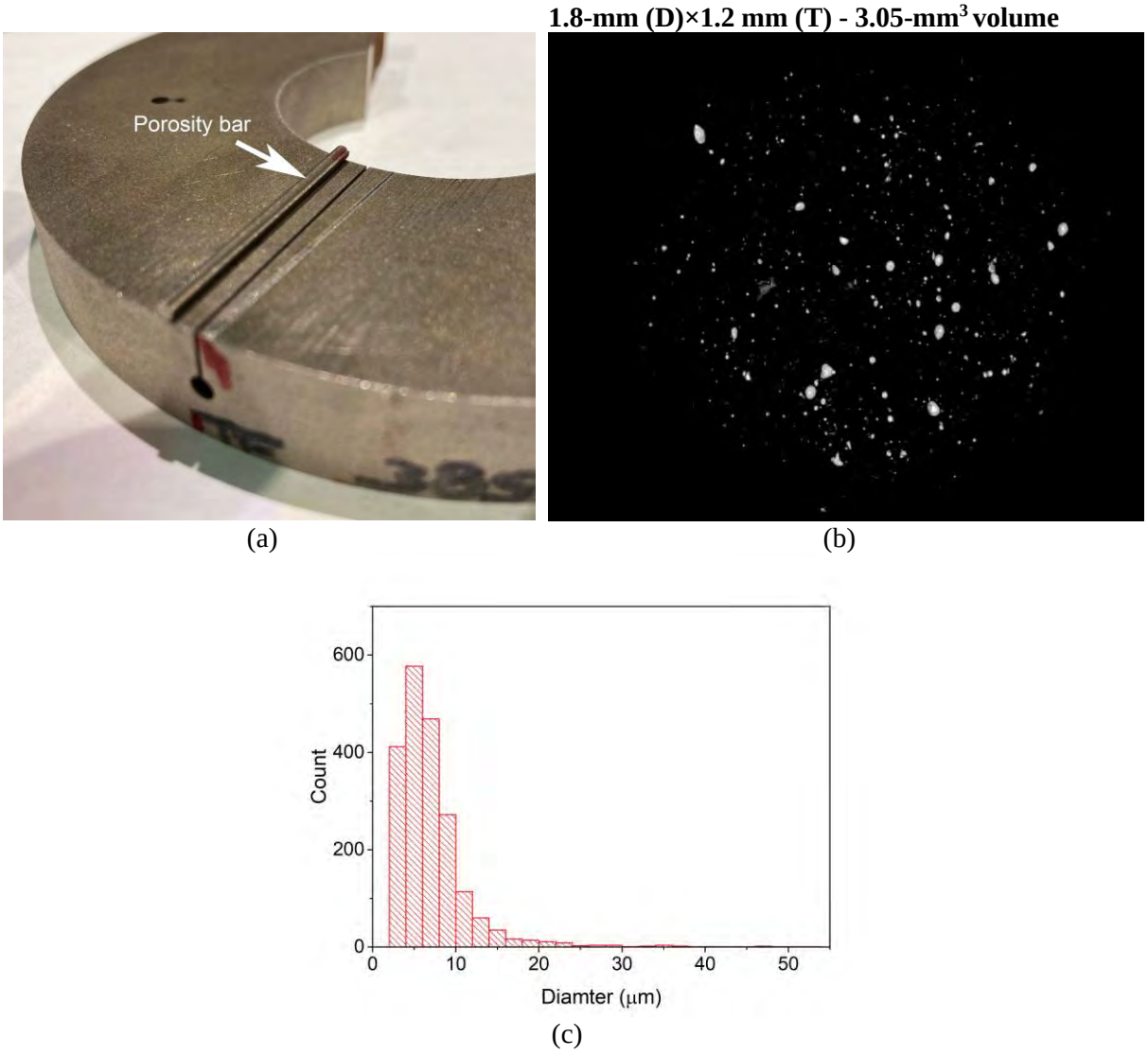


**Figure 20** **(a) Radial bar for porosity measurement at ANL APS; arrow indicates the approximate location of the measurement; (b) image showing pores in the bar in a region close to the ID of the tubing in a 3.05 $mm^3$ volume, (c) size distribution of pores.**

### *3.1.2 Alloy 316L from the flange produced by industry*

The evaluation of porosity by X-ray Tomography at Argonne APS in the flange material produced by industry was conducted in the region to be sampled in SCC CGR test, Figure 5. A 1 mm – dia. bar was extracted in the radial direction in a the same region from where the CT specimens were machined. A total of nine porosity measurements were obtained along the radial direction, each covering 1 mm. One such measurement is shown in Figure 21. The average porosity was calculated over a volume of 7.85 $mm^3$, and was found to be 0.09%, close to the porosity measured for the ANL-produced tubing, Figure 21b. Those values are also close to the HIP + SA condition described in [9]. The average pore size was 5.8 µm (with a 3 µm detection limit), again close to the value measured for the ANL-produced material. The porosity stayed low for the entire 9 mm length that was evaluated, with no discernible trend, Figure 21c.

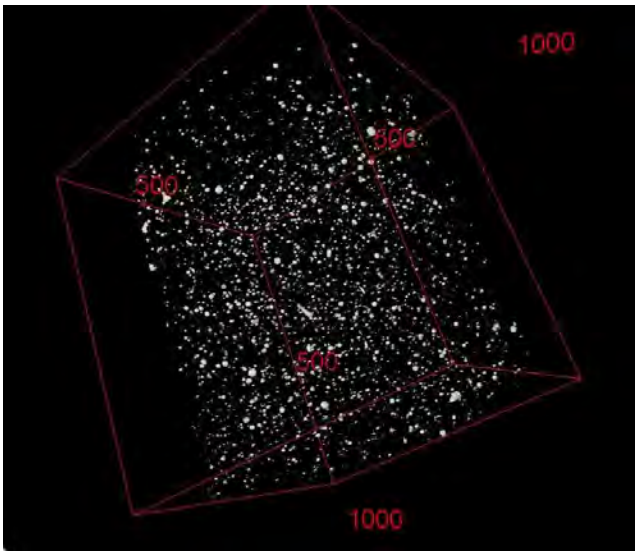


(a)

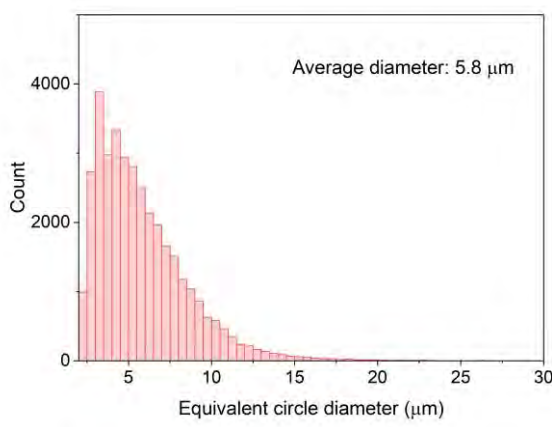


(b)

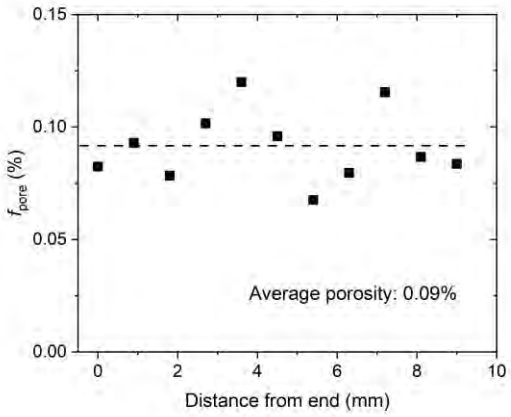


(c)

**Figure 21 (a) Pores in the lower region of the flange from where the CT specimens were extracted in a 0.785 $mm^3$; (b) size distribution of pores; (c) Density of pores along a radial direction.**

### *3.2 SCC Crack growth*

SCC CGR testing involved one specimen, WEC-CT-1 from the Alloy 316L flange supplied by EPRI. The orientations of these specimens with respect to the tubes are shown in Figure 5. From an orientation standpoint, the specimen would correspond to the CR orientation (see Figure 17a).

3.2.1.1 Crack growth rate testing of AM SS316L Specimen WEC-CT-1

The testing conditions for specimen WEC-CT-1 are given in Table 3, and the changes in crack length and $K_{max}$ with time are shown in Figure 22. The test was initiated in simulated PW at 320°C with in-situ precracking (Pre a thru Pre c) followed by transitioning (test periods 1-6). The SCC CGR was evaluated under constant load in test period 7. The overall CGR response was moderate, consistent with measurements conducted under cycle + hold in periods 4 and 5, and previously on ANL-produced material. Next, the cycle + hold conditions were repeated, and a similar response was measured.

**Table 3 Crack growth data in PWR water[a] for AM SS316L Specimen WEC-CT-1.**

| Test Period | Test Time, h | Temp., °C | Load Ratio R | Rise Time, s | Down Time, s | Hold Time, s | $K_{max}$, MPa·m$^{1/2}$ | ΔK, MPa·m$^{1/2}$ | $CGR_{env}$, m/s | Estimated $CGR_{air}$, m/s | Crack Length, mm |
|---|---|---|---|---|---|---|---|---|---|---|---|
| Pre a | 4 | 320.9 | 0.30 | 1 | 1 | 0 | 26.7 | 18.7 | 1.01E-07 | 8.97E-08 | 12.108 |
| Pre b | 8 | 320.8 | 0.30 | 50 | 50 | 0 | 27.0 | 18.9 | 7.61E-09 | 1.85E-09 | 12.172 |
| Pre c | 9 | 319.6 | 0.30 | 2 | 2 | 0 | 27.4 | 19.2 | 7.77E-08 | 4.87E-08 | 12.299 |
| 1 | 11 | 319.8 | 0.50 | 120 | 12 | 0 | 27.5 | 13.8 | 2.11E-09 | 3.34E-10 | 12.326 |
| 2 | 27 | 319.8 | 0.50 | 600 | 12 | 0 | 27.7 | 13.8 | 7.14E-10 | 6.79E-11 | 12.364 |
| 3 | 51 | 319.7 | 0.50 | 1000 | 12 | 0 | 27.9 | 13.9 | 5.64E-10 | 4.16E-11 | 12.412 |
| 4 | 75 | 319.7 | 0.70 | 1000 | 12 | 0 | 28.1 | 8.4 | 1.87E-10 | 9.47E-12 | 12.433 |
| 5 | 101 | 319.4 | 0.70 | 1000 | 12 | 7,200 | 28.2 | 8.5 | 4.97E-11 | 1.16E-12 | 12.439 |
| 6 | 147 | 319.0 | 0.70 | 1000 | 12 | 14,400 | 28.2 | 8.5 | 3.12E-11 | 6.21E-13 | 12.445 |
| 7 | 405 | 319.0 | 1.00 | 0 | 0 | 0 | 28.5 | 0.0 | 1.49E-11 | - | 12.473 |
| 8 | 622 | 318.0 | 0.70 | 1000 | 12 | 14,400 | 28.7 | 8.6 | 2.13E-11 | 6.52E-13 | 12.487 |
| 9 | 1,097 | 318.9 | 0.70 | 1000 | 12 | 7,200 | 28.7 | 8.6 | 1.67E-11 | 1.23E-12 | 12.527 |

[a]Simulated PWR water with 2 ppm Li, 1000 ppm B, and 2 ppm H. DO<10 ppb. Conductivity is 21±3 µS/cm, and pH is 6.4.

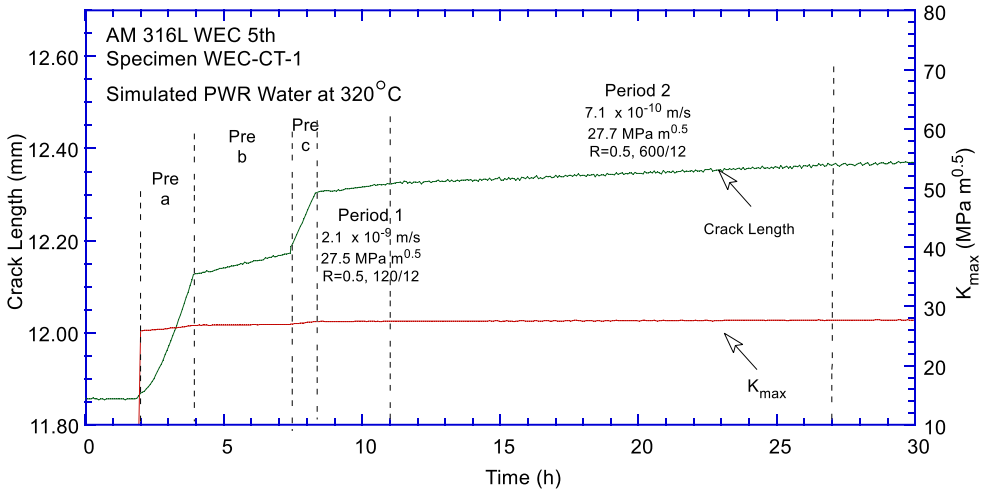


(a)

**Figure 22 Crack length vs. time in simulated PWR environment for AM SS316L Specimen WEC-CT-1 during test periods: (a) precracking-2, (b) 3-4, (c) 5-7, and (d) 8-9.**

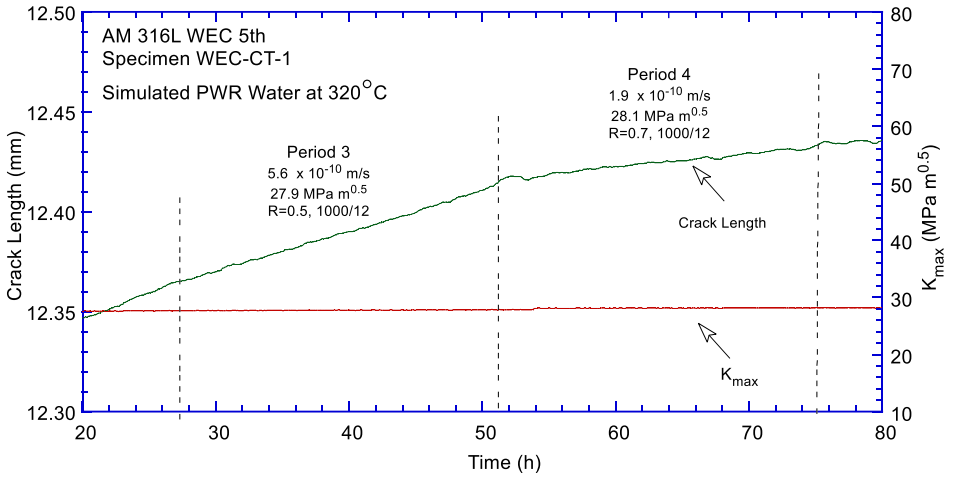


(b)

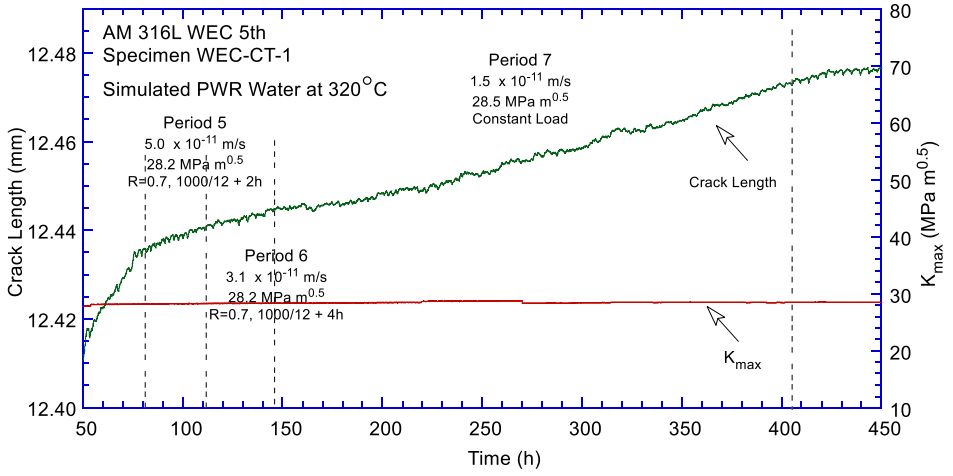


(c)

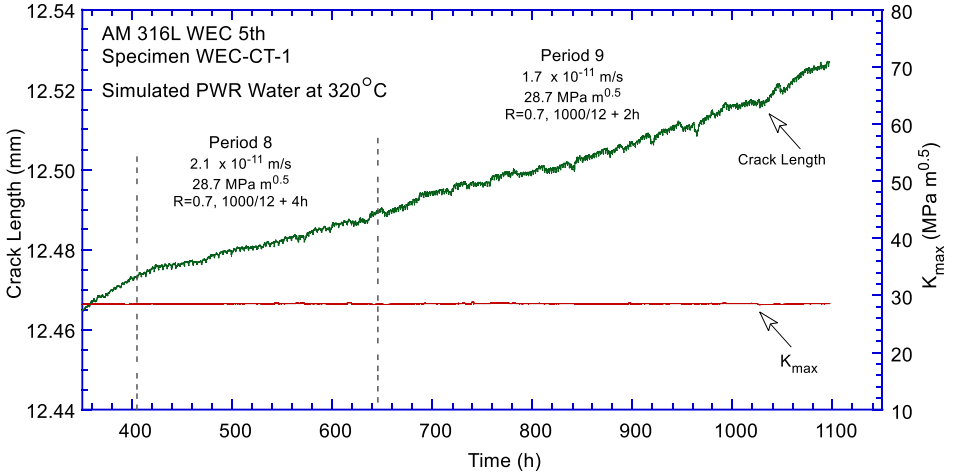


(d)

**Figure 22 (cont.)**

### *3.3 SCC Crack initiation*

In this test, two CT specimens machined from the AM 316L produced at ANL and WEC are loaded under constant load at K ≈ 30 MPa $m^{1/2}$ in series in a "off-normal", aerated PWR environment. The outcome is shown in Figure 23, and shows that unlike a previous specimen with a "as-printed" surface at the notch [22], both machined specimens are resistant to crack initiation. At the time when this report was written, the test was continuing.

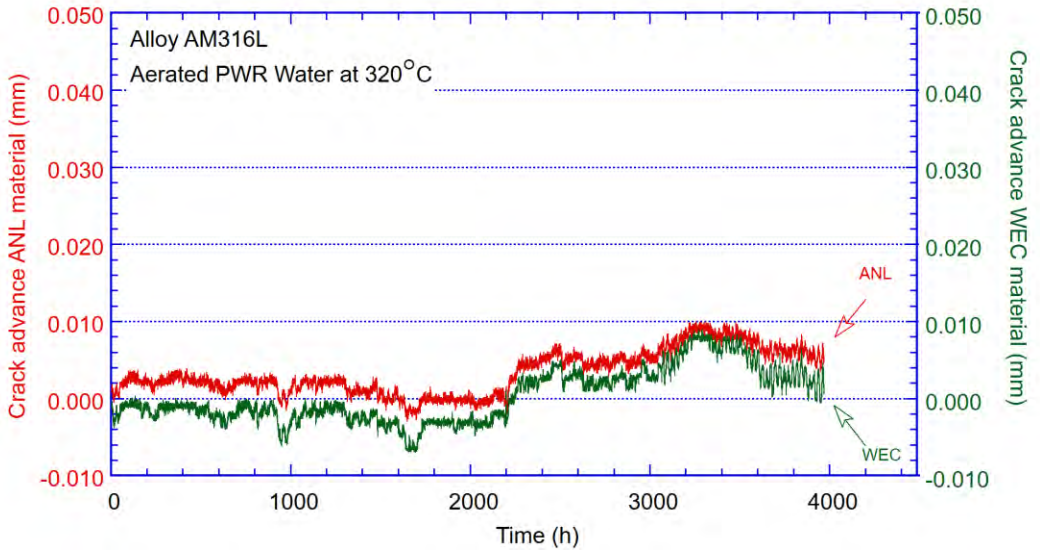


**Figure 23 Crack advance vs. time for specimens machined from AM316L produced by ANL and WEC.**

### *3.4 Fatigue and Environmentally Assisted fatigue*

To assess the performance of AM 316L SS under cyclic loading, fatigue tests were conducted in air and in PWR coolant environment using LPBF materials produced by ANL and WEC. Table 4 summarizes the results obtained from these tests. The temperatures for both the in-air and in-water tests were well controlled, as shown in the table. For the in-water tests, since the compliance of the load train changed continuously under the stroke-controlled test mode, average strain amplitudes and strain rates within the sable ranges of the tests were reported in the table. As expected, the fatigue life of AM316L decreases with increasing strain amplitude in both in-air and in-water tests.

#### *3.4.1 Strain-Life Results*

The strain-life results obtained on the printed tube and flange are shown in Figure 24a. For comparison, the data points obtained from another AM 316L print by a different laboratory are also included [20]. All tests were performed at 300°C either in air or in PWR water. The samples from the printed tube and plates were tested in their as-built (AB), and the samples from the printed flange were tested in their solution annealed (SA) condition. Despite being printed with different LPBF systems and different printing parameters, these AM heats show a similar trend in the strain-life plot when tested in air. At similar strain amplitudes, the fatigue lives of the printed tube obtained in PWR water were a factor of

two lower than that obtained in air, suggesting an environmental effect on fatigue life in PWR water. The fatigue lives of the printed flange in water were even lower. It appears that the SA treatment applied to the printed flange did not improve the cyclic performance of AM 316L SS in PWR water.

A comparison with wrought SS is shown in Figure 24b [23, 24]. The fatigue lives of the AM 316L SS in air are slightly lower than that of wrought SSs at ~300°C. However, given the substantial scatter of fatigue data, the differences are insignificant. In PWR water, AM316L -- both the printed tube and the printed flange -- also fall within the scatter band of wrought SS. These results suggest that, within the tested range, the microstructures of these AM 316L samples, whether in the AB or SA condition, do not have a noticeable impact on their fatigue performance in air or in water. Additional AM data over a broader range of strain amplitudes are still needed to validate this observation.

**Table 4 Fatigue tests performed in air and in PWR water**

| Source of AM materials | Test ID | Sample ID | Environment | Temperature (°C) | Strain AMP [1] (%) | Strain rate [2] (%/s) | Fatigue life (cycles) |
|---|---|---|---|---|---|---|---|
| ANL | LWRS-01 | R745577-01 | Air | 299 | 0.25 | 0.10 | 42,600 |
| | LWRS-02 | R745577-02 | Air | 300 | 0.36 | 0.10 | 14,460 |
| | LWRS-03 | R745577-03 | Air | 300 | 0.46 | 0.10 | 4,990 |
| | EAF-01 | R765768-04 | PWR water | 298 | ~0.33 | ~0.13 | 6,432 |
| | EAF-02 | R765768-01 | PWR water | 299 | ~0.41 | ~0.06 | 2,360 |
| | EAF-03 | R765768-02 | PWR water | 300 | ~0.50 | ~0.07 | 1,250 |
| WEC | EAF-04 | FS-01 | PWR water | 300 | ~0.45 | ~0.06 | 1,019 |
| | EAF-05 | FS-02 | PWR water | 300 | ~0.32 | ~0.06 | 2,655 |
| | EAF-06 | FS-03 | PWR water | 300 | ~0.27 | ~0.06 | 14,650 |

[1, 2] Estimated strain AMP and strain rate for EAF tests in PWR water

### *3.4.2 Cyclic Stress Behavior*

Figure 25a shows the stress amplitudes as a function of cycles for the tests performed on the printed tube in AB condition. At 300°C, all specimens behave similarly regardless of their test environments. Cyclic softening dominates the evolution of stress amplitude beyond a brief transient period at the beginning of the cyclic tests. All samples in AB condition reached their peak stress levels in less than 5 cycles. For the printed flange in SA condition, a short period of cyclic hardening (Figure 25b) can be seen at the beginning of the tests. Within 100 cycles, the cyclic stress-strain curves of the SA material reach their maximum, and start to decline gradually. The rate of cyclic softening is slower for the SA material (i.e., printed flange) than that of AB material (i.e., printed tube).

A higher rate of cyclic softening in the printed tube material may be related to its AB condition since high residual stresses are commonly observed in AM materials without post-built heat treatment. Under cyclic loading, the residual stresses would be relaxed to some extent, leading to cyclic softening. Nonetheless, the stress declines in all tests to a comparable level after ~100 cycles except for the one tested in air at 0.25% strain amplitude (Figure 25a). This low-strain-amplitude test also exhibits secondary hardening at the later stage of the test.

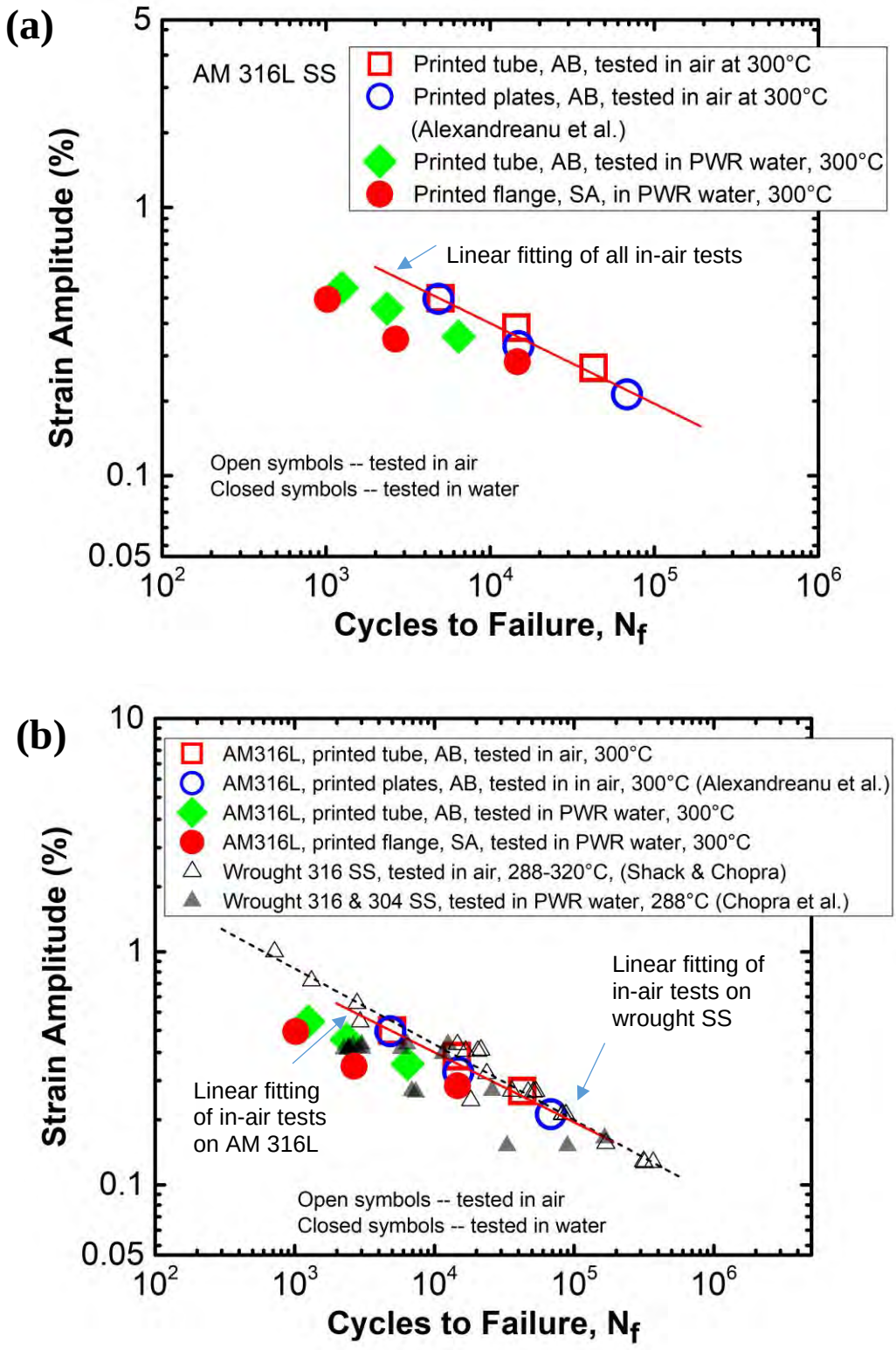


**Figure 24** **Strain-life results of (a) AM 316L SS in AB and SA conditions, and (b) comparison of AM 316L and wrought SS at ~300°C [23, 24].**

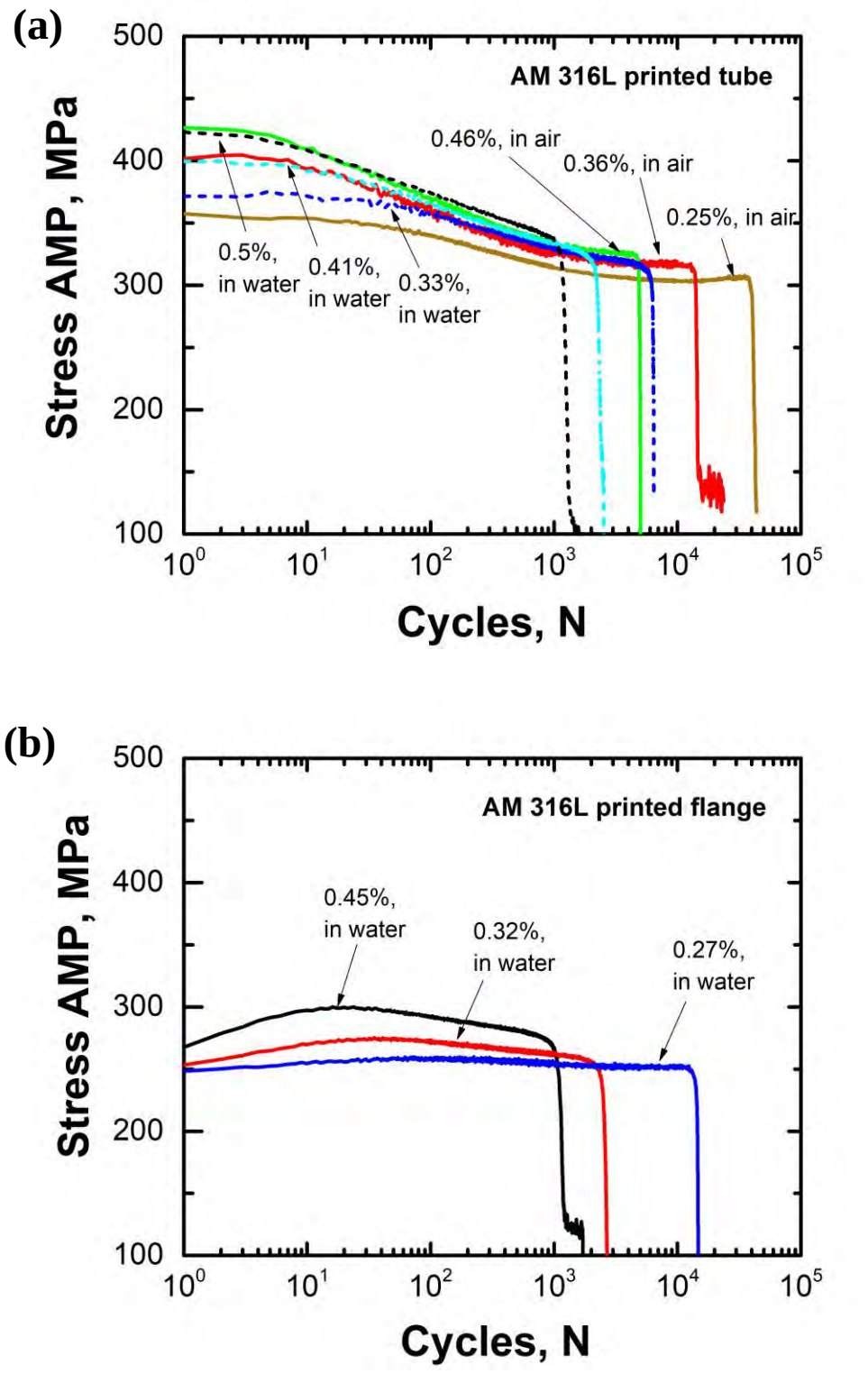


**Figure 25 Stress AMP profiles at 300°C for (a) the printed tube, and (b) the pritned flange.**

# 4 Discussion

## *4.1 Summary of cyclic and SCC CGR data*

Figure 26 summarizes the cyclic CGR data for the two AM 316L alloys tested to date, one produced at ANL and the other supplied by EPRI. For comparison, CGR curves developed for wrought alloys by various institutions, such as ANL [25], Paul Sherrer Institut [26], Bettis Laboratory [27] and Japanese Society of Mechanical Engineers (JSME) [28], are included in the figure. For the initial two tests on ANL produced alloy, Figure 26a, two sets of data were obtained for each specimen at locations at least 1 mm apart. One observes that the CGRs for the alloy in the mechanical fatigue regime ($10^{-8}$-$10^{-7}$ m/s) are exactly as it would be expected for a conventionally produced alloy, i.e., along the 1:1 diagonal. In the corrosion fatigue regime ($10^{-11}$-$10^{-9}$ m/s), there is again no difference between the AM alloy and the conventionally produced SSs. The data shows that the location change – albeit small – did not affect response in either specimen. Also, Figure 26a shows no difference between the two specimens - CR and CL orientations - despite their relative orientation vs. build direction. Figure 26b includes the data obtained on the AM 316L alloy supplied by EPRI. Again, the comparison shows that there is essentially no difference in response between the two AM alloys, and between the AM alloys and the conventionally produced alloys.

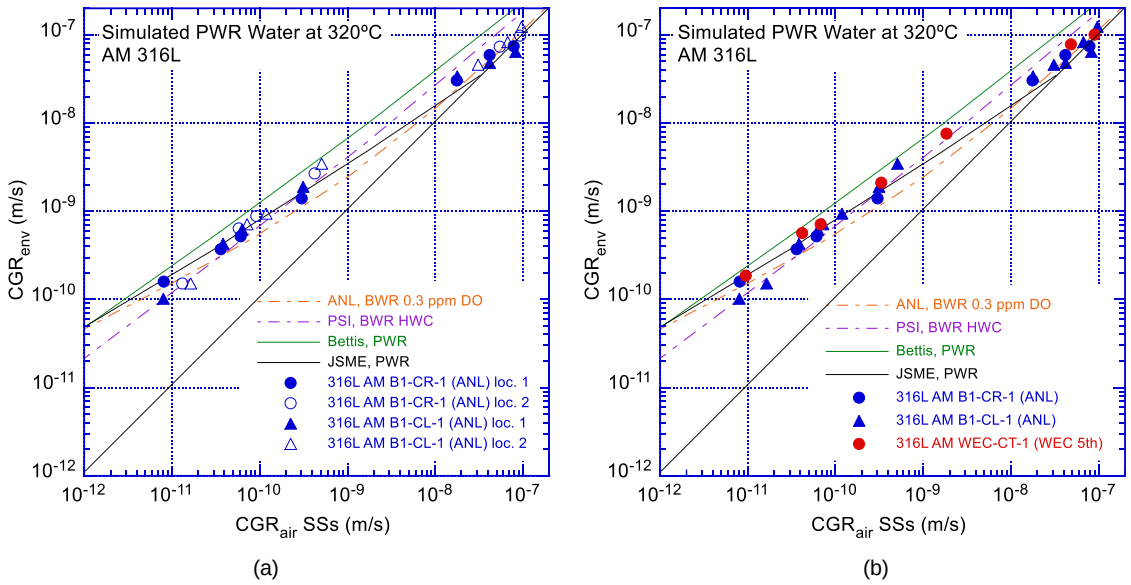


**Figure 26** **Cyclic CGRs measured in the PWR environment vs. CGRs predicted in air under the same loading conditions for AM 316L for specimen (a B1-CR-1 and B1-CL-1 of ANL-produced material, and (b) specimens from both ANL-produced and WEC-produced materials. Also included are CGR curves developed for wrought alloys by various institutions, such as ANL [22], Paul Sherrer Institut [26], Bettis Laboratory [27] and JSME [28]**

Figure 27 shows the SCC CGR data vs K for AM 316L alloys, one produced at ANL and one produced by WEC and supplied by EPRI. The ANL alloy was tested in the as-built condition (porosity 0.06%) while the material supplied by EPRI had an SA treatment post-build, but a very similar porosity of 0.09%. Also included in the figure are data for wrought and cast SS material along with the NUREG-

0313 disposition curve [11]. Overall, the SCC CGR response of AM materials seems similar to each other and to that of the conventional alloys.

As described previously, both AM 316L specimens proved to be resistant to SCC. This data demonstrates that the use of AM alloys in a nuclear environment is plausible, however, concerns remain with regard to the heterogeneity and anisotropy of the AM materials, an issue that would be better addressed by testing multiple specimens of varying porosities.

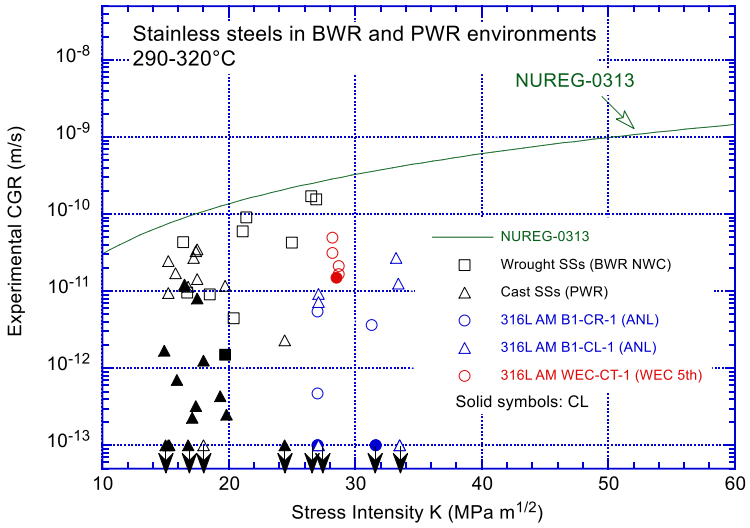


**Figure 27** **SCC CGR data vs K for AM 316L produced at WEC and at ANL. Closed symbols represent data obtained under constant load while open symbols represent data obtained under periodic partial unloading (PPU) conditions. Also included wrought and cast SS data as well as the NUREG-0313 CGR curve.**

### *4.2 Crack initiation*

In this FY's test, two CT specimens machined from the AM 316L produced at ANL and WEC have been tested in series in a "off-normal", aerated PWR environment. The outcome (Figure 23) shows that unlike a previous specimen with a "as-printed" surface at the notch [22], both machined specimens are resistant to crack initiation.

Figure 28 summarizes the previous crack initiation results with printed AM 316L specimens with "as-printed" and "machined" notches. In the first test, two CT specimens printed in a similar orientation, i.e., with the notches pointing up (indicated by red arrows in Figure 28a), and differing only at the notch surface – "as printed" vs "machined"- were tested in series in an aerated PWR environment and showed that the "as-printed" surface is more likely to initiate and grow a crack than the machined surface. As the SCC CGR of specimen labelled "1UP" reached 2.5 x $10^{-11}$ m/s, the test was stopped. In the second test, two CT specimens printed in a similar orientation, i.e., with the notches pointing down (indicated by blue arrows in Figure 28a), and differing only at the notch surface – "as printed" vs "machined"- proved resistant. These results suggest that the specimens printed with the notch pointing down were more resistant to SCC initiation than the specimens with the notch pointing up. The effect suggests that printing geometry affects local susceptibility to cracking, and the "unsupported" arches such as those of

notched pointing up can lead to vulnerabilities. The finding – if supported by future additional observations – suggests that printing unsupported geometries should be avoided. Also, the first test seems to suggest that in cases where susceptibility exists, the as-printed surface initiated cracking faster than the machined surface.

(a)

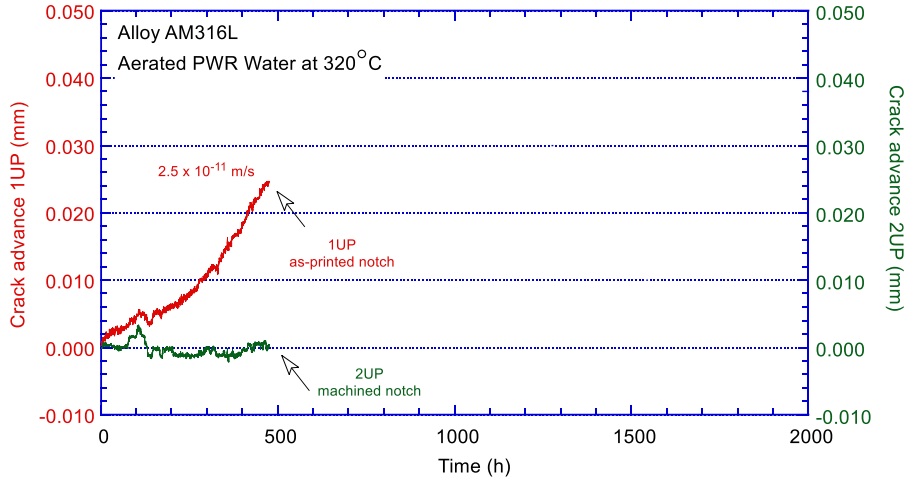


(b)

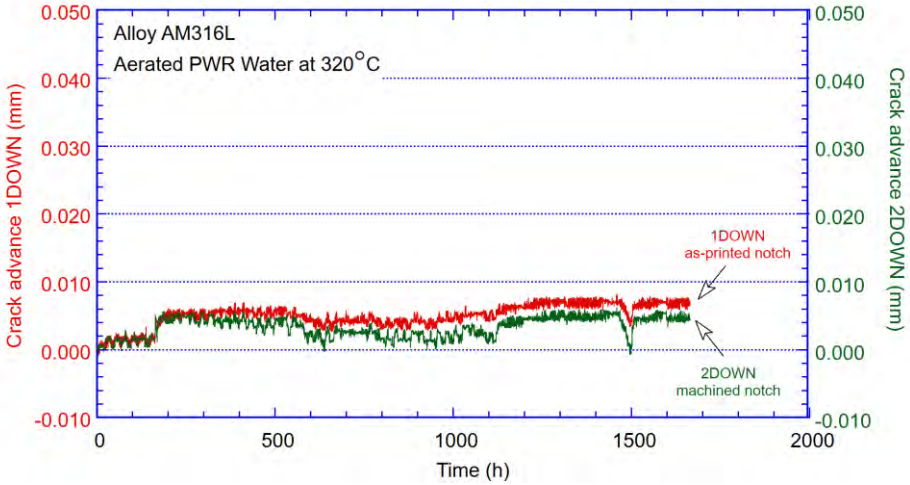


(c)

**Figure 28** **(a) CGR/crack initiation compact tension specimens printed using the Renishaw AM400 LPBF system. Specimens with similar geometry, printed with the notch "UP" (red) or "DOWN" (blue), differing only at notch - "as printed" vs "machined" - are evaluated for crack initiation simultaneously. (b) Crack advance vs. time for AM316L (a) "UP" specimens, and (b) "DOWN" specimens differing only at notch - "as printed" vs "machined".**

Since AM components are expected to be produced near-net-shape, the effect of surface finish (as printed vs. machined) on fatigue and SCC crack initiation will require additional evaluation.

### *4.3 Environmentally assisted fatigue*

The ASME Code fatigue design curves, which are based primarily on strain-controlled tests in air, provide the allowable number of cycles as a function of applied stress amplitude. However, the effects of environments on the fatigue performance of materials are not addressed in the ASME fatigue design curves. To incorporate the environmental effects, a correction factor ($F_{en}$) has been proposed to account for the negative impact of environment on fatigue life [23, 24]. The $F_{en}$ is defined as the ratio of the fatigue life in air at room temperature to the fatigue life in water at the service temperature. While both fatigue and environmental fatigue data are scarce for AM 316L SS, the same $F_{en}$ approach can be used to assess the environmental effect on AM materials.

Figure 29 shows the strain-life results of AM316L SS and the ASME Code curves developed for wrought austenitic SSs. Within the strain range explored in this study, the data points of the in-air tests (open symbols in the figure) are slightly below the ASME mean curve for wrought SSs. The best fit curve of the AM316L data deviates more from the ASME mean curve with the increase of strain amplitude. Nonetheless, the data points obtained from the in-water tests (i.e., the close symbols for printed tube and flange) are lower than those of the in-air tests, but remain above the ASME Code design curve for wrought SSs.

To assess the effects of PWR water on the fatigue performance of AM 316L, environmental fatigue correction factors ($F_{en}$) were estimated for both the printed tube and flange materials using the ASME Code mean curve as the reference (Table 5). Because AM materials exhibit slightly lower fatigue lives than wrought SS, this approach is expected to yield somewhat higher $F_{en}$ valves. The calculated $F_{en}$ for the AM samples span a wide range, from 2.8 to 7.8. Differences in fatigue behavior between the AM and wrought materials -- rather than environmental effects -- likely contributed to this spread. To isolate the environmental contribution to fatigue performance in AM alloys, a mean curve developed with only AM fatigue data would be needed.

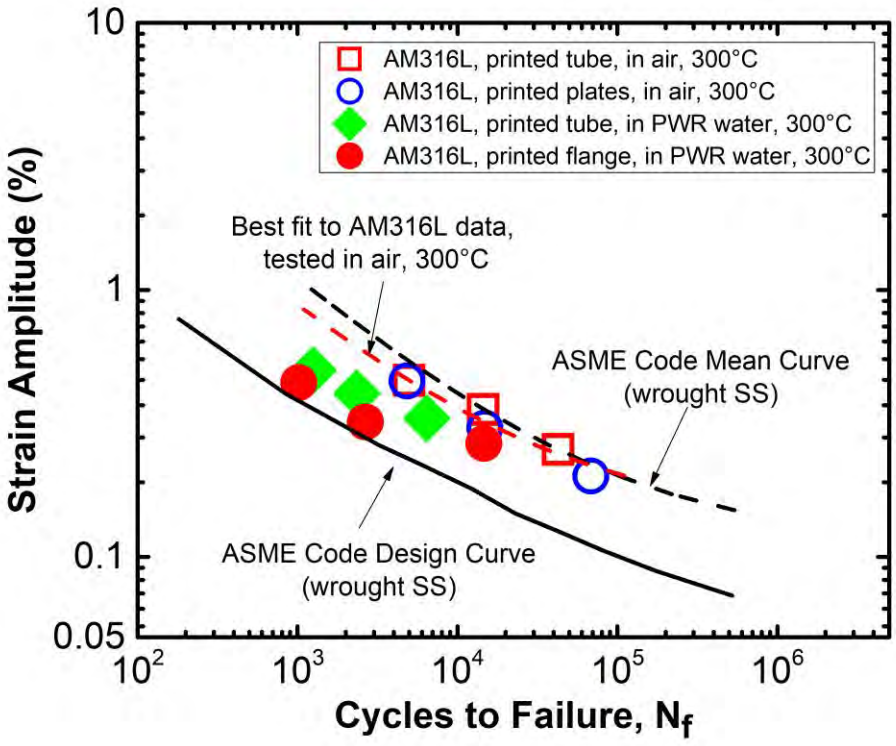


**Figure 29 Strain-life data for AM 316L SS compared to ASME Code Mean and Design Curves for wrought SS.**

With available data for wrought and cast austenitic SSs, the key material, loading, and environmental parameters influencing fatigue life were analyzed in NUREG/CR-6909 R1[24]. Correlations for estimating the fatigue lives of wrought and cast SSs in LWR environments were developed, and the $F_{en}$ value of SSs can be expressed as a function the transformed temperature (T*), DO level (O*), and strain rate ( $\dot{\varepsilon}^*$),

$$\boldsymbol{F_{en} = \exp(-T^* O^* \dot{\varepsilon}^*)}, \quad (1)$$

where T*, O*, and $\dot{\varepsilon}^*$ are defined as:

$$\begin{aligned} \boldsymbol{T^* &= 0} && \boldsymbol{(T < 100°C)} \\ \boldsymbol{T^* &= (T - 100)/250} && \boldsymbol{(100°C \le T \le 325°C)} \end{aligned} \quad (2)$$

$$\begin{aligned} \boldsymbol{O^* &= 0.29} && \boldsymbol{(DO < 0.1\ ppm)} \\ \boldsymbol{O^* &= 0.29} && \boldsymbol{(DO > 0.1\ ppm,\ \text{sensitized high-carbon SSs})} \\ O^* &= 0.14 && (DO > 0.1\ ppm,\ \text{not sensitized}) \end{aligned} \quad (3)$$

$$\begin{aligned} \boldsymbol{\dot{\varepsilon}^* &= 0} && \boldsymbol{(\dot{\varepsilon} > 7\%/s)} \\ \boldsymbol{\dot{\varepsilon}^* &= Ln(\dot{\varepsilon}/7)} && \boldsymbol{(0.0004\%/s \le \varepsilon \le 7\%/s)} \\ \boldsymbol{\dot{\varepsilon}^* &= Ln(0.0004/7)} && \boldsymbol{(\dot{\varepsilon} < 0.0004\%/s)} \end{aligned} \quad (4)$$

Using Eqs. (1-4), $F_{en}$ values were calculated for the AM 316L samples tested in PWR water. As shown in Table 5, the results are all around 3, except one test that was conducted at a higher strain rate. These $F_{en}$ values are comparable to those of wrought SSs tested in the same LWR environment, suggesting that the same $F_{en}$ correlations are applicable to AM materials under simulated LWR water. Additional room-temperature, in-air fatigue tests are still needed to establish an AM-specific mean curve without environment. Relative to such an AM baseline, $F_{en}$ values estimated using the ASME Code mean curve would be overestimated by approximately a factor of 1.5–2.5.

**Table 5 Estimated environmental correction factor for AM316L SS**

| | **Strain AMP (%)** | **Strain rate (%/s)** | **Estimated environmental correction factor** | |
|---|---|---|---|---|
| | | | Estimated with the ASME mean curve for wrought SS in air at RT | Estimated with temperature, DO, and strain rate |
| Printed tube in AB condition | 0.33 | 0.13 | 2.8 | 2.5 |
| | 0.41 | 0.07 | 4.3 | 3.0 |
| | 0.5 | 0.07 | 4.8 | 2.9 |
| Printed flange in SA condition | 0.45 | 0.06 | 7.8 | 3.0 |
| | 0.32 | 0.06 | 7.6 | 3.0 |
| | 0.27 | 0.06 | 2.4 | 3.0 |

# 5 Summary

The performance of AM 316L in simulated water coolant and high temperature air was evaluated. For this purpose, materials from printed component-like structures were examined and tested. The microstructural examination focused on porosity and was measured by computed tomography at ANL APS. Testing involved SCC initiation, SCC crack growth and EAF. The research and outcomes are summarized as follows:

- This past fiscal year, the performance of AM 316L in a light water environment was evaluated using material from an industry (WEC) -produced AM flange printed using an EOS M290 Laser Powder Bed Fusion (LPBF) system. The data complements that obtained from tubing printed and tested at ANL using a Renishaw AM400 LPBF. These geometries are intended to act as surrogates for complex components where nuclear equipment vendors are more likely to consider AM technologies.
- The porosity of the WEC flange material was measured of approximately 9 mm along the radial direction and was found to be small, 0.09% - very similar to the porosity measured in ANL-produced tubing - with only small variations along that direction.
- SCC CGR testing revealed that the fatigue and corrosion fatigue CGR response of industry (WEC)-built flange material was found to be similar to that on the ANL-built material and that expected for conventional alloys. Similar to the ANL-produced alloys, the WEC-produced alloy was also resistant to SCC growth.
- Crack initiation tests suggest that machined surfaces are resistant to SCC initiation in both ANL and WEC printed material. However, previous results have shown that printing geometry affects local susceptibility to cracking, i.e., “unsupported” arches such as those of notched pointing up can lead to vulnerabilities. The finding – if supported by future additional observations – suggests that printing unsupported geometries should be avoided. Also, initial testing seems to suggest that in cases where susceptibility exists, the as-printed surface initiated cracking faster than the machined surface. Since AM components are expected to be produced near-net-shape, the effect of surface finish (as printed vs. machined) on fatigue and SCC crack initiation will require additional evaluation.
- The fatigue performance of AM materials was evaluated in simulated PWR environment. The fatigue lives of the industry-built flange material were similar to that of ANL-built tubing material, and they were both lower than the fatigue lives in air. While cyclic softening dominated the stress evolution for both ANL- and industry-produced AM 316L SS, a short period of cyclic hardening can be seen in industry-produced AM material with post-print SA treatment. Nonetheless, the SA treatment did not improve the fatigue performance of AM 316L SS. Based on the approach proposed in NUREG-6909 for wrought and cast austenitic SSs, the estimated environmental correction factor ($F_{en}$) for AM316L SS is about 3 in PWR water. This value is comparable to those for conventional alloys. Given that fatigue performance of AM materials is slightly worse than that of their wrought counterparts, a similar effect of environmental enhancement is expected on the fatigue behavior for wrought and AM 316L SSs..

## References


1. International Energy Agency. 2019. Nuclear Power in a Clean Energy System, https://www.iea.org/reports/nuclear-power-in-a-clean-energy-system.
2. U.S. Energy Information Administration. 2021. “Primary Energy Production by Source.” accessed August 30, 2021. Sourced from: https://www.eia.gov/totalenergy/data/browser/.
3. Electric Power Research Institute, 2021. Leveraging Existing Infrastructure – Nuclear Power, Paper for Summer Seminar 2021
4. K.A. Terrani “Accelerating the Deployment of Advanced Nuclear Energy Systems.” Nuclear News, Apr. 2020, 34-37.
5. Roadmap for Regulatory Acceptance of Advanced Manufacturing Methods in the Nuclear Energy Industry, Nuclear Energy Institute, May 13, 2019.
6. D.W. Gandy, Strategy/approach for qualification of nuclear components produced via additive manufacturing, in: US DOE Advanced Methods of Manufacturing Workshop, US Department of Energy, Germantown, MD, USA, 2016.
7. A. Hiser, NRC Perspectives on Advanced Manufacturing Technologies, GAIN Advanced Manufacturing for Nuclear Workshop, December 4, 2018.
8. M. Audrain, NRC Technical Assessment of Additive Manufacturing –Laser Powder Bed Fusion, NRC Workshop on Advanced Manufacturing Technologies for Nuclear Applications December 9, 2020.
9. Xiaoyuan Lou, Miao Song, Paul W. Emigh, Michelle A. Othon, Peter L. Andresen, "On the stress corrosion crack growth behavior in high temperature water of 316L stainless steel made by laser powder bed fusion additive manufacturing", Corrosion Science, 128, pp 140-153, 2017
10. Xiaoyuan Lou, Michelle A. Othon, Raul B. Rebak, "Corrosion fatigue crack growth of laser additively-manufactured 316L stainless steel in high temperature water", Corrosion Science, 127, pp 120-130, 2017.
11. W.S. Hazelton, “Technical report on material selection and processing guidelines for BWR coolant pressure boundary piping”, NUREG-0313-Rev2, 1986.
12. D. Gandy, S. Tate, M. Albert, C. Armostrong, 316L Stainless Steel Manufactured via Laser Powder Bed Fusion Additive Manufacturing Data Package & Code Case, in: U.S. NRC Workshop on Advanced Manufacturing Technologies for Nuclear Applications December 9, 2020. ML20344A011.
13. V. Nikitin. TomocuPy – efficient GPU-based tomographic reconstruction with asynchronous data processing. Journal of Synchrotron Radiation, 30(1):, Jan 2023. URL: https://doi.org/10.1107/S1600577522010311, doi:10.1107/S1600577522010311.
14. American Society for Testing and Materials, “Standard Test Method for Measurement of Fatigue Crack Growth Rates,” ASTM E647-08, DOI 10.1520/E0647-08, West Conshohocken, PA, 2008.
15. American Society for Testing and Materials, “Standard Test Method for Determining a Threshold Stress Intensity Factor for Environment-Assisted Cracking of Metallic Materials,” ASTM E1681-03, DOI 10.1520/E1681-03R08, West Conshohocken, PA, 2008.
16. Electric Power Research Institute, “PWR Primary Water Chemistry Guidelines,” Volume 1, Revision 4, EPRI, Palo Alto, CA, 1999.
17. N. Huin, personal communication, 2023.
18. M. Herbst, R. Kilian, N. Huin and O. Calonne, " SCC of Austenitic Stainless Steels Under Off-Normal Water Chemistry and Surface Conditions, Part II: Off Normal Chemistry—Long Term Oxygen Conditions and Oxygen Transients", Proc. of the 18th Int. Conf. on Environmental

Degradation of Materials in Nuclear Power Systems – Water Reactors, The Minerals, Metals & Materials Series, https://doi.org/10.1007/978-3-030-04639-2_55.
19. American Society for Testing and Materials, “Standard Test Method for Strain-Controlled Fatigue Testing,” ASTM E606/E606M-21, DOI:10.1520/E0606_E0606M-21, West Conshohocken, PA, 2021.
20. Alexandreanu, B., X. Zhang, Y. Chen, W.-Y. Chen and M. Li. "Mechanical Testing of Additively Manufactured Materials", Argonne National Laboratory, ANL/NSE-22/83, 2022.
21. M. Li, X. Zhang, W.Y. Chen, T.S. Byun, Creep behavior of 316 L stainless steel manufactured by laser powder bed fusion, J. Nucl. Mater., 548 (2021), Article 152847.
22. Alexandreanu, B., Y. Chen, and X. Zhang, “Performance Testing of Additively Manufactured 316L Stainless Steel in Light Water Reactor Environment”, Argonne National Laboratory, ANL/LWRS-24/3, 2024.
23. O. K. Chopra, and Shack, W. J., 1998, “Effects of LWR Coolant Environments on Fatigue Design Curves of Carbon and Low-Alloy Steels,” NUREG/CR-6583, ANL-97/18.
24. O. K. Chopra, and G. L. Stevens, “Effect of LWR Coolant Environments on the Fatigue Life of Reactor Materials—Final Report,” NUREG/CR-6909. Rev.1, May 2018.
25. Shack, W. J., and T. F. Kassner, “Review of Environmental Effects on Fatigue Crack Growth of Austenitic Stainless Steels,” NUREG/CR–6176, ANL–94/1, May 1994.
26. H.P. Seifert and S. Ritter, Environmentally-Assisted Cracking in Austenitic Light Water Reactor Structural Materials, PSI Bericht Nr. 09-03, March 2009, ISSN 1019-0643.
27. G.F. Li, J. Congleton, *Corrosion Science*, 42, pp. 1005 – 1021, 2000.
28. S.L. Hong et al., "Measurements of stress corrosion cracking growth rates in weld Alloy 182 in primary water of PWR", Proc. of the 10th Int. Conf. on Environmental Degradation of Materials in Nuclear Power Systems – Water Reactors, Houston, TX: NACE, 2001, CDROM.

This page intentionally left blank


Nuclear Engineering Division
Argonne National Laboratory
9700 South Cass Avenue, Bldg. 208
Argonne, IL 60439

www.anl.gov